Journal of Constructional Steel Research 245 (2026) 110531

Contents lists available at ScienceDirect

Journal of Constructional Steel Research

journal homepage: www.elsevier.com/locate/jcsr

Probabilistic buckling analysis of suction bucket foundations for offshore wind turbines using non-homogeneous random fields

M. Fina [a,*], M. Böhm [b], S. Freitag [a], P. Schaumann [b], E. Ghafoori [b]

[a] Karlsruhe Institute of Technology, Institute for Structural Analysis, Kaiserstr. 12, 76131 Karlsruhe, Germany
[b] Leibniz University Hannover, Institute for Steel Construction, ForWind, Appelstr. 9A, 30167 Hannover, Germany

ARTICLE INFO

Dataset link: https://doi.org/10.25835/jn1a6pxa

Keywords:
Buckling analysis
Suction buckets
Offshore wind turbines
Random fields
Geometric imperfections
Non-homogeneity

ABSTRACT

Suction bucket foundations are increasingly used for offshore wind turbines in combination with jacket substructures due to their noise-free installation and reduced embedment depth. However, the design of their thin-walled cylindrical skirts is driven by buckling due to negative pressure. Geometric imperfections have a significant influence on the buckling behavior. Due to inherent uncertainty, identifying geometric imperfections that represent realistic imperfections is challenging. Consequently, large reduction factors are applied in combination with very unfavorable imperfection patterns to account for uncertainties, which often results in conservative designs with higher material consumption. The uncertainty of geometric imperfections can be quantified using random fields, which are often assumed to be homogeneous, with constant statistical behavior across the shell surface.

Based on experimental imperfection data from lab-scale and full-scale suction buckets, it is demonstrated that geometric imperfections of suction buckets are characterized by non-homogeneity. Probabilistic buckling analyses are performed using non-homogeneous random fields as geometric imperfections applied to finite element models of suction buckets. The proposed approach generates imperfection patterns that are similar to the measured imperfection patterns. Results show that the mean buckling pressures from the non-homogeneous approach closely match the experimental results and are less conservative than those obtained from the classical homogeneous random field approach and from design buckling pressures according to Eurocode 3. The findings emphasize the influence of non-homogeneous random imperfection modeling on probabilistic buckling loads and indicate the potential for less conservative and more efficient skirt designs. This paper contributes to advanced probabilistic design methodologies for shell structures.

1. Introduction

Offshore wind energy has a key role within the European Union's ambitious climate goals in the transition to a sustainable energy system [1]. Potential offshore development areas in Europe have moderate water depths, making them suitable for fixed-bottom structures. With increasing turbine size, the trend shifts towards the installation of jacket structures, which have lower weight and higher stiffness compared to monopiles. In connection with suction bucket foundations, it is possible to develop areas where the soil conditions do not allow pile installation. Suction buckets consist of a cylindrical shell, the so-called skirt, and a lid. The shell diameter is relatively large, while the required skirt length is significantly shorter than the pile length for the same location. Another major advantage is the low noise emission during the installation, compared to typically applied impact driving. For the installation, water pumps are used to create a pressure difference within the foundation, which forces the suction buckets into the seabed. The suction bucket design, and in particular the skirt thickness, is driven by the installation load case. The negative pressure on the skirt and lid can lead to shell buckling of the structure during the installation. The buckling capacity of these thin-walled shells is highly sensitive to imperfections, which can significantly reduce the load-bearing capacity. To predict the buckling capacity of suction buckets, the structure and its surrounding soil are numerically modeled. In current engineering practice, the conventional design approach for suction bucket foundations is based on geometrically and materially non-linear analyses with imperfections (GMNIA), where the FE model also includes the soil. The GMNIA approach for the verification of shell stability is described in Eurocode 3 (EC3): EN 1993-1-6 [2]. Since the surrounding soil creates a complex, 'non-linear' boundary condition, it is not possible to find an analytical solution for the ideal elastic buckling stress and apply the

* Corresponding author.
E-mail address: marc.fina@kit.edu (M. Fina).

https://doi.org/10.1016/j.jcsr.2026.110531
Received 12 December 2025; Received in revised form 2 June 2026; Accepted 15 June 2026
Available online 26 June 2026

generalized buckling capacity curve and reduction factors described in EC3 [2]. The semi-analytical approach described in DNV-RP-C202 [3] is also only applicable to shells with idealized boundary conditions. The calibration of an equivalent unsupported length of the shell with idealized boundary conditions is very challenging, as it depends on soil type, stiffness and the flow regime due to the installation. The Eurocode 3 requires the application of the most unfavorable equivalent geometric imperfection form. In practice, buckling modes derived from a linear bifurcation analysis are typically implemented as imperfection forms. However, these do not reflect measured imperfections like weld depressions and ovalizations, which result from the manufacturing process. Depending on the detailed design, the imperfections can also be distributed in a non-homogeneous manner over the length of the shell. Series production, which is common in the offshore sector, makes it possible to measure imperfections and thus form a basis for the generation of more 'realistic' imperfection forms. The application of 'realistic' manufacturing imperfections instead of 'worst' imperfections would lead to smaller wall thicknesses of the skirt for the same installation pressure and thus to a more economic design.

However, the imperfection patterns can vary from shell to shell, even within the same batch. The modeling of this inherent uncertainty is challenging, especially when only a few measurements are available. Therefore, traditional design concepts often require large reduction factors also known as knockdown factors (KDFs) to account for uncertainty [4], which often leads to a conservative design with increased material usage. Accordingly, the development of reliable and more economical KDFs is still part of numerous research projects, see, for example, [5–12]. Some of the aforementioned studies aim to enhance safety factors through the application of probabilistic methods. In [6,13,14], the first-order second-moment (FOSM) method is used for probabilistic shell buckling design. In this approach, measured geometric imperfections are represented by Fourier series, with the Fourier coefficients defined as random variables. A Taylor series is used for estimating the second-order statistics of the buckling load. In [15], a Fourier approach to model random imperfections of a full-scale suction bucket is presented.

Alternatively, spatially varying imperfections can be modeled using random fields based on autocorrelation functions. The methods applied in shell buckling can be categorized into spectral representation method using the evolutionary power spectrum [16–18] and spectral decomposition of the covariance structure [19–21]. A commonly used approach for the spectral decomposition is the Karhunen–Loève expansion (KLE). Böhm [22] uses the KLE to generate homogeneous Gaussian random fields for the buckling analysis of suction buckets. The correlation parameters of a random field significantly influence the stochastic buckling response, as quantitatively investigated using the KLE in [23]. Defining the parameters based on limited experimental data is challenging. The concept of polymorphic uncertainty modeling [24] allows for the consideration of both uncertainty characteristics: aleatory and epistemic uncertainty. Aleatory uncertainty is the natural variability, observed in the variations of measured imperfections between shells. This uncertainty characteristic cannot be reduced and is modeled with random variables or random fields. Epistemic uncertainty is related to limited knowledge, e.g., incomplete or imprecise data and is modeled with interval and fuzzy variables. To consider this lack of knowledge in the probabilistic modeling of geometric imperfections, the concept of polymorphic uncertainty for shell buckling is proposed in [25–28]. In this approach, the correlation parameters of the random field are defined by interval and fuzzy variables. Further studies on the concept of polymorphic uncertainty in shell buckling have explored various aspects, including a sensitivity analysis of correlation parameters in [29], a novel shell design concept based on a fuzzy-valued safety level in [30], efficient surrogate modeling strategies to reduce the computation times of stochastic buckling analysis involving random fields [31,32] and buckling design optimizations accounting for both aleatory and epistemic uncertainty in [33–36].

Several assumptions are required when generating shell imperfections using random field theory, including whether the field is homogeneous or non-homogeneous, and whether it follows a Gaussian or non-Gaussian distribution. Due to simplification, it is often assumed that geometric deviations of shells are homogeneous and Gaussian distributed. The influence of possible non-homogeneous and non-Gaussian distributions is neglected. A random field is non-Gaussian distributed when the random variables at each point do not follow a Gaussian distribution. In [37], stochastic non-Gaussian material and thickness properties are considered, and in [38,39] geometric imperfections are modeled as non-Gaussian random fields. A non-homogeneous random field occurs when its mean, variance, or autocorrelation structure varies spatially [40]. Non-homogeneous fields are frequently applied in soil mechanics to characterize the non-homogeneous nature of the spatial variability of soil parameters; see, e.g., [41–43]. To the best of the authors' knowledge, only limited literature exists that addresses the need for non-homogeneous random field models in shell buckling. For example, in [44], non-homogeneous characteristics of initial imperfections of lab-scale axially compressed cylinders from aerospace are described using the spectral representation method. The results indicate that accounting for non-homogeneous random imperfections yields buckling load predictions that closely align with experimental results. In [45], measured geometric imperfections of a full-scale suction bucket are presented, revealing that the smoothness of the imperfection field varies along the length of the shell. At the top, where the lid is welded, the amplitude of the imperfections decreases, while at the bottom, where the bucket is embedded in the seabed, larger amplitudes and a wavy shape are observed. This characteristic non-homogeneity, shaped by the manufacturing process, should not be modeled using homogeneous random fields.

This paper focuses on modeling the spatial non-homogeneity of geometric imperfections of suction buckets for offshore wind turbines. Different non-homogeneous random field approaches are introduced to consider the manufacturing process. The non-homogeneity is modeled with non-homogeneous variance functions, whereas the correlation model remains homogeneous. The advancement of imperfection modeling using random field approaches depends on the availability of imperfection data. Therefore, the variance and correlation functions are derived from imperfection measurements of lab- and full-scale suction buckets, which are available open access at https://doi.org/10.25835/jn1a6pxa. A probabilistic buckling analysis is performed, where the random imperfections are generated using the KLE. The results are compared with those obtained using a homogeneous random field approach and with the buckling design loads specified in Eurocode 3 (EC3) [2]. Furthermore, conducting finite element (FE) computations for the elastic–plastic buckling limit state of cylindrical shells presents a particular challenge [46]. This challenge requires careful consideration of multiple modeling choices, such as selecting suitable shell elements with moderate or finite rotations, balancing mesh refinement against computational cost, choosing path-following methods that can robustly capture highly non-linear behavior, the definition of a reliable criterion to identify a stability point (e.g., eigenvalue problems, the determinant or negative diagonal elements of the tangent stiffness matrix), and, as discussed above, considering the various possibilities of imperfection modeling, among others. Therefore, the buckling load responses are validated through experiments and compared using different FE programs from academia and industry: FEAP and ABAQUS. In addition, the numerical results are verified with analytical solutions. The paper aims to enhance the stochastic modeling of spatially varying geometric imperfections for suction buckets. The main contributions can be summarized as follows:

- Development of non-homogeneous random field approaches for suction bucket imperfection modeling
- Evaluation of measured imperfection data of lab- and full-scale shells for random field modeling

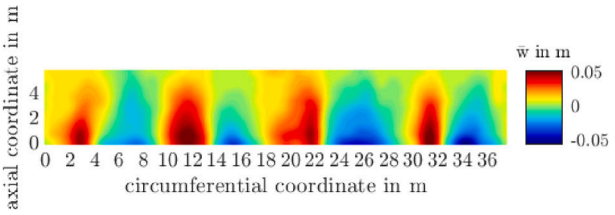

Fig. 1. Measured imperfection according to LeBlanc Bakmar [45].

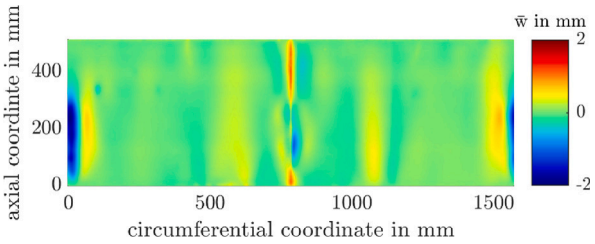

Fig. 2. Measured imperfection of lab-scale specimen 1 [22].

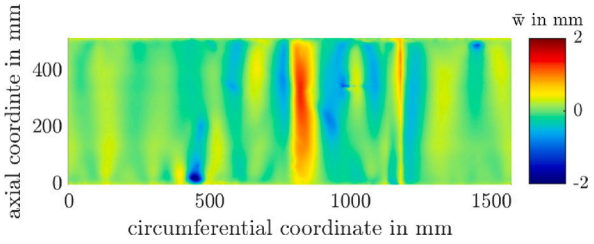

Fig. 3. Measured imperfection of lab-scale specimen 2 [22].

- Validation of the buckling load responses with experimental buckling tests
- Comprehensive probabilistic buckling analysis of lab- and full-scale suction buckets based on measured imperfection data
- Comparison of the numerical results using FE programs from academia and industry: FEAP and ABAQUS
- Proposal of a less-conservative fully probabilistic design approach for suction buckets

In Section 2, experimental imperfection data from one full-scale and two lab-scale suction buckets are evaluated and represented using truncated Fourier series. Based on this data, correlation functions and non-homogeneous variance approaches are developed in Section 3. In Section 4, Finite element models of lab- and full-scale suction buckets are constructed in ABAQUS and FEAP, and subsequently compared, experimentally validated, and analytically verified. Results of the probabilistic buckling analysis for both the homogeneous and non-homogeneous Gaussian random field approaches are then presented and compared with experimental results and design guidelines in Section 5. Finally, conclusions and directions for future research are presented in Section 6.

2. Evaluation of experimental data of geometric imperfections

2.1. Geometric imperfection data

Geometric imperfections of cylindrical shells are defined as deviations in the radial direction from the nominal shell surface. The full-scale suction bucket used in this study was measured using a high-resolution laser scan of a 'Mobile Met Mast' published by [45], which was constructed in Aalborg, Denmark, in 2008. The dimensions of the bucket foundation are $L = 6\,\text{m}$, $r = 6\,\text{m}$ and $t = 20\,\text{mm}$, with a maximum measured imperfection amplitude of 112 mm [45]. The imperfection amplitude is defined as the distance between the maximum and minimum deviations from the nominal surface (peak-to-peak amplitude). The largest imperfections are found near the four welds in the meridional direction. The measured imperfections $\bar{w}$ are shown in Fig. 1. The lab-scale measurements are from two of the test specimens scanned and tested within the ProBucket project [47]. The specimens have an outer diameter of 500 mm, a shell length of 506 mm and a thickness of 0.75 mm. On the top and bottom are welded end plates with a thickness of 9 mm and a diameter of 504 mm. Both specimens have one longitudinal weld on the shell and several dimples. The specimens were scanned by the project partner Fraunhofer IWES with an ATOS Q system by GOM with an in-plane resolution of 0.124 mm. The maximum imperfection of specimen 1 is due to an intentionally created dimple at the circumferential coordinate of 0 mm with an amplitude of $\Delta w_{0\theta} = -1.95\,\text{mm}$, shown in Fig. 2. The largest imperfection of specimen 2 is an inward dimple with $\Delta w_{0\theta} = -2.01\,\text{mm}$ at a transportation-related dent at the bottom end of the shell, displayed in Fig. 3.

2.2. Description of imperfection with Fourier series

The measured geometric imperfections of shells can be treated as a two-dimensional field. Decomposing the imperfection pattern into a truncated Fourier series proved to be an efficient way to describe this field mathematically [48]. The main advantage of this description is independent of a mesh with a certain fidelity, and the data size is significantly reduced. The classical formulation of a discrete two-dimensional Fourier series can only describe periodic functions. For the circumferential direction of cylinders, this is an advantage, but in the axial direction, the field is non-periodic. Hence, a common way of dealing with this issue is to modify the Fourier series to yield the so-called 'half-wave cosine' approach, first introduced by Arbocz [49]. In the axial direction, a symmetry with $2L$ is assumed, which allows different imperfection amplitudes on the edges, and reduces deviations from the original function, compared to a periodic basis function. The approximated geometric imperfection with the half-wave cosine formulation is written as

$$\hat{w}(x,y) = 2t \sum_{k=0}^{n_x} \sum_{l=0}^{n_y} \cos\left(\frac{k\pi x}{L}\right)\left(A_{kl}\cos\left(\frac{ly}{r}\right) + B_{kl}\sin\left(\frac{ly}{r}\right)\right), \tag{1}$$

where t is the shell thickness, $2L$ and $2\pi r$ are the periods in the y and x directions, and A_{kl} and B_{kl} are Fourier coefficients corresponding to k half waves in the axial and l full waves in the circumferential direction. The total number of half waves n_x and full-waves n_y have an influence on the accuracy of the approximation.

For this formulation, the Fourier coefficients of the measured geometric imperfection are determined by

$$A_{kl} = \frac{\alpha}{\pi L} \sum_{x=-L}^{L} \sum_{y=0}^{2\pi r} \bar{w}(x,y)\cos\left(\frac{k\pi x}{L}\right)\cos\left(\frac{ly}{r}\right)\Delta x \Delta y \tag{2}$$

and

$$B_{kl} = \frac{\alpha}{\pi L} \sum_{x=-L}^{L} \sum_{y=0}^{2\pi r} \bar{w}(x,y)\cos\left(\frac{k\pi x}{L}\right)\sin\left(\frac{ly}{r}\right)\Delta x \Delta y, \tag{3}$$

where $\bar{w}$ are the measured deviations in the radial direction from the nominal shell surface depending on the axial x and circumference coordinate y, which are depicted in Figs. 1–3 for the full-scale and the two specimens of the lab-scale suction buckets, respectively. The numerical substitution factor α is defined based on the number of half waves in the axial direction k and the number of full waves in the circumferential direction l as

$$\alpha = \begin{cases} 4, & \text{if } k > 0 \text{ and } l > 0 \\ 2, & \text{if } k > 0 \text{ or } l > 0 \\ 1, & \text{if } k = 0 \text{ and } l = 0. \end{cases} \tag{4}$$

It is conventional to normalize the Fourier coefficients by the shell wall thickness and then further adjust the measured imperfection amplitude to the desired amplitude by scaling the Fourier coefficients. The corresponding Fourier coefficients are available open access in a data repository at https://doi.org/10.25835/jn1a6pxa. The provided coefficients are calculated for the full-scale suction bucket, scaled to a maximum imperfection amplitude of 119.5 mm. In contrast, the lab-scale shells are not pre-scaled. Studies on the accuracy of the Fourier series approximation are presented in [22], where a convergence study with increasing numbers of axial and circumferential modes was conducted to achieve a close match of the predicted buckling pressure.

3. Random field modeling of geometric imperfections

In this section, random field modeling for geometric imperfections is discussed when the imperfection data show non-homogeneous properties. First, the basics of random field theory and their discretization using the KLE are provided. Then, different approaches are proposed to generate non-homogeneous random imperfections based on the available imperfection measurements. Finally, a correlation model used to assess the correlation properties from imperfection measurements is presented.

3.1. Basics of homogeneous random fields

In the following, a brief summary of the fundamentals of random field modeling based on [50–52] is provided. Random fields are used to model the spatial aleatory uncertainty of geometric shell imperfections, where the random field describes the random geometric deviations of the shell surface coordinates. Thus, the field of random deviations (geometric imperfections) $i\hat{w}(\boldsymbol{x},\theta)$ is, in a mathematical sense, a collection of random variables defined as

$$\{i\hat{w}(\boldsymbol{x},\theta) \mid \boldsymbol{x}\in\Omega,\theta\in\Theta\},\quad \boldsymbol{x}=\begin{pmatrix} x \\ y \end{pmatrix}. \tag{5}$$

The possible outcomes within the event set Θ are labeled as θ. A random variable $i\hat{w}(\boldsymbol{x}_0,\theta)$ is assigned to a fixed location $\boldsymbol{x}_0\in\Omega$. If a Gaussian random field is present, each point is associated with a Gaussian normal distribution, characterized by mean $\mu(\boldsymbol{x})$ and variance $\sigma^2(\boldsymbol{x})$

$$i\hat{w}(\boldsymbol{x}_0,\theta)\sim\mathcal{N}(\mu(\boldsymbol{x}_0),\sigma^2(\boldsymbol{x}_0)). \tag{6}$$

Furthermore, a specific realization of a random field corresponding to a given event θ_0 can be indicated as

$$i\hat{w}_0(\boldsymbol{x}) := i\hat{w}(\boldsymbol{x},\theta_0). \tag{7}$$

The autocovariance function, which describes the covariances of two points $\boldsymbol{x}_i=(x_i,y_i)$ and $\boldsymbol{x}_j=(x_j,y_j)$, is defined as

$$C(\boldsymbol{x}_i,\boldsymbol{x}_j)=E[(i\hat{w}(\boldsymbol{x}_i)-\mu(\boldsymbol{x}_i))(i\hat{w}(\boldsymbol{x}_j)-\mu(\boldsymbol{x}_j))], \tag{8}$$

which can be normalized with the standard deviations $\sigma(\boldsymbol{x}_i)$ and $\sigma(\boldsymbol{x}_j)$, leading to the autocorrelation function

$$\rho(\boldsymbol{x}_i,\boldsymbol{x}_j)=\frac{C(\boldsymbol{x}_i,\boldsymbol{x}_j)}{\sigma(\boldsymbol{x}_i)\sigma(\boldsymbol{x}_j)}. \tag{9}$$

A random field is referred to as weakly homogeneous when its first two moments (mean and variance) remain constant throughout the domain Ω

$$\mu(\boldsymbol{x})=\mu\quad\text{and}\quad\sigma^2(\boldsymbol{x})=\sigma^2. \tag{10}$$

In addition, a homogeneous covariance function is defined as

$$C(\boldsymbol{x}_i,\boldsymbol{x}_j)=C(d)=\sigma^2\rho(d), \tag{11}$$

where the autocorrelation function (acf) $\rho(d)$ is rotation invariant, which means it depends only on the relative distance d between the two points $\boldsymbol{x}_i$ and $\boldsymbol{x}_j$. Under this assumption, the random field can also be regarded as isotropic. Typically, the distance d is computed using the Euclidean distance between the two points

$$d(\Delta x,\Delta y)=\sqrt{\Delta x^2+\Delta y^2}=\sqrt{(x_j-x_i)^2+(y_j-y_i)^2}, \tag{12}$$

with the distances in the axial direction Δx and in the circumferential direction Δy of the two points on the shell surface. To numerically generate random fields, a discretization technique is required. One common approach is the KLE, which provides a series expansion of the weakly homogeneous random field in discrete form. The KLE series is defined by

$$i\hat{w}(\boldsymbol{x},\theta)=\mu+\sum_{i=1}^{N}\sqrt{\lambda_i}\,\xi_i(\theta)\,\varphi_i(\boldsymbol{x}), \tag{13}$$

where $\xi_i(\theta)\sim\mathcal{N}(0,1)$ is a standard normally distributed random variable, $\varphi_i(\boldsymbol{x})$ is the ith eigenfunction and λ_i is the corresponding ith eigenvalue obtained by solving the eigenvalue problem

$$\boldsymbol{C}\,\boldsymbol{\varphi}_i=\lambda_i\,\boldsymbol{\varphi}_i, \tag{14}$$

where the covariance matrix

$$\boldsymbol{C}=\begin{bmatrix} C(\boldsymbol{x}_1,\boldsymbol{x}_1) & \dots & C(\boldsymbol{x}_1,\boldsymbol{x}_j) & \dots & C(\boldsymbol{x}_1,\boldsymbol{x}_N) \\ \vdots & \ddots & \vdots & \ddots & \vdots \\ C(\boldsymbol{x}_i,\boldsymbol{x}_1) & \dots & C(\boldsymbol{x}_i,\boldsymbol{x}_j) & \dots & C(\boldsymbol{x}_i,\boldsymbol{x}_N) \\ \vdots & \ddots & \vdots & \ddots & \vdots \\ C(\boldsymbol{x}_N,\boldsymbol{x}_1) & \dots & C(\boldsymbol{x}_N,\boldsymbol{x}_j) & \dots & C(\boldsymbol{x}_N,\boldsymbol{x}_N) \end{bmatrix}, \tag{15}$$

is calculated by Eq. (11) based on the FE mesh with N nodes. For large FE models, a significant number of eigenvalues and eigenfunctions have to be computed and stored, which is computationally intensive. Therefore, a truncation of the KLE series is recommended for large-scale problems. As outlined in [23], a reduced number of eigenvalues and eigenfunctions $M<N$ is considered, such that their sum accounts for $Q=99\,\%$ of the total eigenvalue sum. In [53], Q is interpreted as a quality index

$$Q=\frac{1}{\mathrm{tr}(\boldsymbol{C})}\sum_{i=1}^{M}\lambda_i\quad\text{with}\quad\mathrm{tr}(\boldsymbol{C})=\sum_{i=1}^{N}C_{ii}=\sum_{i=1}^{N}\lambda_i, \tag{16}$$

using the fact that the trace of the covariance matrix $\mathrm{tr}(\boldsymbol{C})$ is equal to the sum of the eigenvalues λ_i. The truncation of the KLE series can be significantly reduced depending on the correlation properties of the imperfection field. The less correlated the field, the more terms are required. As an example, for the homogeneous random fields considered later for the full-scale suction bucket, the dimensionality can be reduced from $N=217\times70=15190$ (equal to the number of FE nodes) to only $M=64$ terms. Consequently, the computational cost is significantly reduced, especially with respect to the storage of eigenvalues and eigenvectors.

3.2. Simulation of non-homogeneous random geometric imperfections

In the literature, the terms non-homogeneous and non-stationary are often used synonymously. Therefore, in this study, a random field is referred to as non-homogeneous (i.e., non-stationarity in space) when its second order statistics (mean and variance) vary across the domain Ω. The non-homogeneity of geometric imperfections is modeled through spatially varying variance functions. However, the correlation structure depends only on the relative distance between points and not on their absolute locations. This means that the correlation structure remains homogeneous. Accordingly, non-homogeneous random imperfections can be simulated using the Karhunen–Loève expansion given in Eq. (13) as

$$i\hat{w}(\boldsymbol{x},\theta)=\sigma(\boldsymbol{x})\sum_{i=1}^{M}\sqrt{\lambda_i}\,\xi_i(\theta)\,\varphi_i(\boldsymbol{x}), \tag{17}$$

with respect to the reduced number of M eigenvalues and eigenvectors. The mean value μ in Eq. (13) is set to zero. A spatially varying

Table 1
Overview of the proposed variance approaches.

Variance model	Function
hom	$\sigma_n^2(x,y) = \hat{\sigma}_n^2$
non-hom 1	$\sigma_n^2(x,y) = \hat{\sigma}_n^2 \;\; \hat{\sigma}_n^2(x)$
non-hom 2	$\sigma_n^2(x,y) = \hat{\sigma}_n^2 \;\; \hat{\sigma}_n^2(x) \;\; \hat{\sigma}_n^2(y)$

mean would imply a change in the reference radius of the cylinder. However, imperfections are defined as geometric deviations from a fixed reference surface. Consequently, only the variance $\mathrm{Var}(\boldsymbol{x}) = \sigma^2(\boldsymbol{x})$, and thus the standard deviation $\sigma(\boldsymbol{x}) = \sqrt{\mathrm{Var}(\boldsymbol{x})}$, vary across the shell surface. The spatially varying standard deviation can be multiplied in front of the sum in Eq (17). Then, the variance in Eq (11) no longer needs to be considered, and the covariance matrix is constructed using only the autocorrelation function: $C(\boldsymbol{x}_i, \boldsymbol{x}_j) = C(d) = \rho(d)$.

3.2.1. Variance approaches

The variance function on the shell surface of the nth specimen is defined as

$$\sigma_n^2(x,y) = \hat{\sigma}_n^2 \;\; \hat{\sigma}_n^2(x) \;\; \hat{\sigma}_n^2(y), \tag{18}$$

where the constant sample variance $\hat{\sigma}_n^2$ is independent of the shell coordinates and can be calculated for each specimen by

$$\hat{\sigma}_n^2 = \frac{1}{N-1} \sum_{k=1}^{N} (\hat{w}_n(x_k, y_k) - \bar{\mu}_n)^2 \tag{19}$$

with $\bar{\mu}_n$ denoting the sample mean of the complete geometric imperfection field. This field is represented as a Fourier series $\hat{w}_n(x_i, y_i)$ according to Eq. (1), and evaluated at the $N = N_x \times N_y$ nodes of the FE mesh.

It is assumed that the geometric imperfections can be described by two independent one-dimensional stochastic processes: $\hat{w}(y_i)$ with $i \dots N_y$ observations at FE nodes in the circumferential direction and $\hat{w}(x_j)$ with $j \dots N_x$ observations at the FE nodes in the axial direction. Based on this assumption of separability, the mutually independent variance function in the axial direction is given by

$$\sigma_n^2(x_j) = \frac{1}{N_y - 1} \sum_{i=1}^{N_y} \left(\hat{w}_n(x_j, y_i) - \bar{\mu}_n^y\right)^2 \tag{20}$$

and in the circumferential direction defined by

$$\sigma_n^2(y_i) = \frac{1}{N_x - 1} \sum_{j=1}^{N_x} \left(\hat{w}_n(x_j, y_i) - \bar{\mu}_n^x\right)^2 \tag{21}$$

with the sample mean values $\bar{\mu}_n^y$ and $\bar{\mu}_n^x$ corresponding to the number of samples N_y and N_x, respectively. Furthermore, both functions are normalized by their maximum values as

$$\hat{\sigma}_n^2(x) = \frac{\sigma_n^2(x)}{\|\sigma_n^2(x)\|_\infty} \quad \text{and} \quad \hat{\sigma}_n^2(y) = \frac{\sigma_n^2(y)}{\|\sigma_n^2(y)\|_\infty} \tag{22}$$

in the non-homogeneous variance model defined in Eq. (18). It should be noted that the variance function in Eq. (18) is anisotropic, as it can be expressed in terms of two independent functions, $\hat{\sigma}_n^2(x)$ and $\hat{\sigma}_n^2(y)$, in the x- and y-directions.

Finally, when multiple shell specimens are available per batch, the mean variance function is computed as the average across all specimens in the batch

$$\bar{\sigma}^2(x,y) = \frac{1}{N_{\text{spec}}} \sum_{n=1}^{N_{\text{spec}}} \sigma_n^2(x,y) \tag{23}$$

with the number of specimens per batch N_{spec}. All proposed variance models are summarized in Table 1. Thus, random geometric imperfections are generated, and an extensive study of the stochastic buckling behavior is conducted in Section 5. In addition to the homogeneous approach "hom", two non-homogeneous approaches, "non-hom 1" and "non-hom 2", are distinguished, which differ in the direction-dependence of the variance. The "non-hom 1" approach is proposed to simulate random imperfections whose non-homogeneity is particularly pronounced in the axial direction (x), as observed in the full-scale suction bucket. When, in addition, as seen in the lab-scale shells, a pronounced variation of the variance in the circumferential direction (y) is observed, the 'non-hom 2' approach can be selected.

The mean variance functions for each variance model are calculated according to Eq. (23) based on a grid of $N = 120 \times 40$ nodes. For the full-scale suction bucket ($N_{\text{spec}} = 1$) the three variance models are depicted in Fig. 4. The variance model "hom" is used to generate homogeneous random geometric imperfections. This model exhibits a constant variance of $\bar{\sigma}^2(x,y) = 4.84 \times 10^{-4}\,\text{m}^2$ across the entire domain. In contrast, model "non-hom 1" shows a strong non-homogeneous behavior. The variance function decreases along the axial direction from the bottom at $x = 0$ to the top at $x = 11\,\text{m}$ of the suction bucket. Additionally, model "non-hom 2" accounts for the waviness of the variance in the circumferential direction. The observation of this distinct non-homogeneity and its influence on the buckling behavior motivates the present paper. Moreover, variance functions from the two lab-scale shells ($N_{\text{spec}} = 2$) are analyzed. The mean variance functions, according to Eq. (23), are also computed on a grid of $N = 120 \times 40$ nodes for the three different variance models and are shown in Fig. 5. The homogeneous model "hom" shows a constant variance of $\bar{\sigma}^2(x,y) = 0.072\,\text{mm}^2$. In contrast to the models for the full-scale bucket, the non-homogeneous models "non-hom 1" and "non-hom 2" of the lab-scale buckets do not show a pronounced increase or decrease in variance along the axial direction. It is noteworthy that the variance model "non-hom 2" reduces the variance to zero across large areas of the domain. Finally, it should be noted that the welding of bucket foundations may include both transverse and longitudinal seams. To avoid stress concentration at the welds, misalignment between these seams can occur. This effect can be represented using the "non-hom 2" model, in which the alignment of the welds in both directions can be described by the variance function.

3.2.2. Correlation model

The covariance function in Eq (11) depends only on the distance and is therefore homogeneous. Similar to the variance model described by Eq. (18), the assumption of separability holds. This implies that the imperfections along the x (axial) and y (circumferential) directions are statistically independent, and the covariance function depends only on the lags Δx and Δy. Thus, the covariance function can be written as

$$C(\Delta x, \Delta y) = \bar{\rho}_n(\Delta x)\, \bar{\rho}_n(\Delta y) \tag{24}$$

without the spatially varying variance $\sigma^2(\boldsymbol{x})$, which is included in Eq. (17) as the standard deviation. The function in Eq. (24) represents a correlation model with two one-dimensional autocorrelation functions $\bar{\rho}_n(\Delta x)$ and $\bar{\rho}_n(\Delta y)$ along the axial (x) and circumferential (y) coordinates of the nth cylindrical shell. This fully separable correlation model is proposed by [20] under the assumption that both autocorrelation functions are independent. Fina et al. [25–28] extend the model by introducing a fuzzy correlation structure to account for epistemic uncertainties. These contributions present an approach for calculating the autocorrelation functions $\rho_n(\Delta x)$ and $\rho_n(\Delta y)$ based on measured geometric imperfections, which are represented as Fourier series. The correlation structure is anisotropic, as different functions are employed for $\rho_n(\Delta x)$ and $\rho_n(\Delta y)$. However, it remains homogeneous because it does not depend on the absolute location, but only on the distances Δx and Δy.

A sample of the one-dimensional autocorrelation function in the axial direction $\rho(\Delta x = \xi \Delta x_0)$ for a specific circumferential coordinate y_i can be calculated as

$$\rho_i(\xi \Delta x_0) = \frac{1}{N_x} \sum_{j=1}^{N_x - \xi} (w(x_j + \xi \Delta x_0, y_i) - \bar{\mu}_n)(w(x_j, y_i) - \bar{\mu}_n) \tag{25}$$

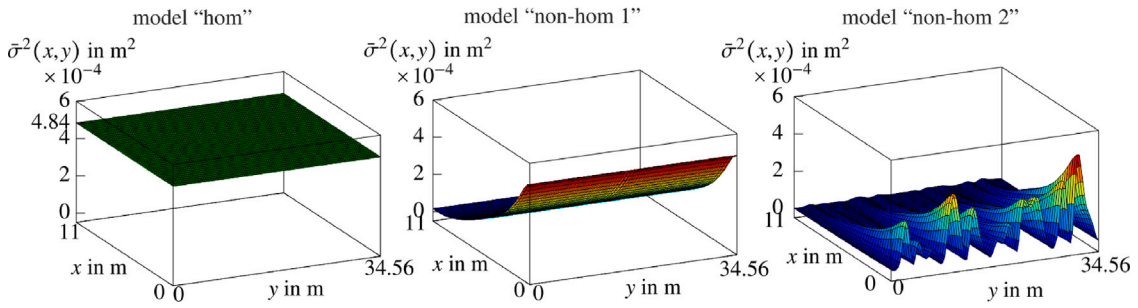

Fig. 4. Variance models of the full-scale suction bucket: the homogeneous model "hom" (left) and the non-homogeneous models "non-hom 1" (middle) and "non-hom 2" (right).

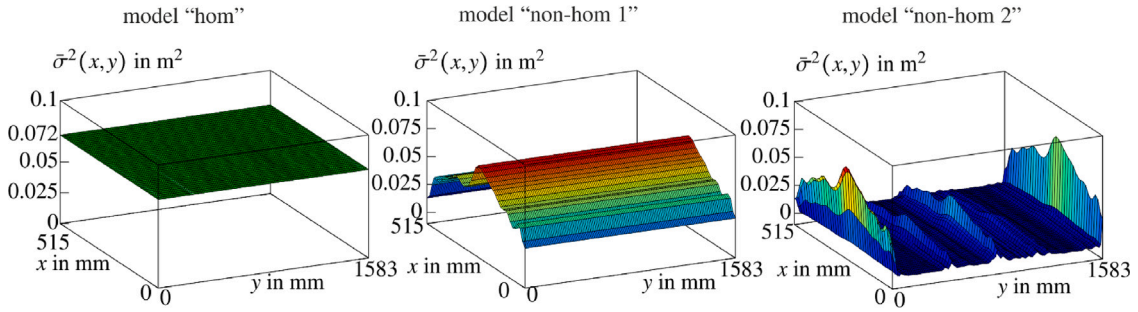

Fig. 5. Variance models of the lab-scale suction bucket: the homogeneous model "hom" (left) and the non-homogeneous models "non-hom 1" (middle) and "non-hom 2" (right).

with $\xi = 0 \ldots N_x - 1$ denoting the multiple of the constant lag Δx_0. It should be emphasized that the autocorrelation function is a biased estimator scaled by $1/N_y$ [27]. In the examples of this study, the random field is defined on a regular finite element (FE) mesh. Thus, the lag Δx_0 corresponds to the element length in the axial direction. Furthermore, the one-dimensional autocorrelation function in the circumferential direction, $\rho(\Delta y = \eta \Delta y_0)$, for a specific axial coordinate x_j, is defined as

$$\rho_j(\eta \Delta y_0) = \frac{1}{N_y - 1} \sum_{i=1}^{N_y - 1} (w(x_j, y_i + \eta \Delta y_0) - \bar{\mu}_n)(w(x_j, y_i) - \bar{\mu}_n) \tag{26}$$

with $\eta = 0, \ldots, N_y - 1$ denoting integer multiples of the constant lag Δy_0. It should be noted that the number of lags, and therefore the upper limit of the summation, has to be fixed to $N_y - 1$, since the cylinder is closed and the seam node is removed.

To evaluate the sample autocorrelation function for the entire specimen, ensemble averaging is applied with the assumption that one sample with its stochastic information represents the whole set. This assumption of ergodicity is allowed when the random field or process (in this case, the imperfection field) can be decomposed into statistically independent components along the axial and circumferential directions. This condition is already assumed by the fully separable correlation model given by Eq. (24), as introduced at the beginning of this Section 3.2.2. Consequently, the axial autocorrelation function is computed by averaging the circumferential samples

$$\bar{\rho}_n(\xi \Delta x_0) = \frac{1}{N_y} \sum_{i=1}^{N_y} \rho_i(\xi \Delta x_0), \tag{27}$$

and the circumferential autocorrelation function by averaging across the axial samples

$$\bar{\rho}_n(\eta \Delta y_0) = \frac{1}{N_x} \sum_{j=1}^{N_x} \rho_j(\eta \Delta y_0). \tag{28}$$

This leads to the ensemble autocorrelation function $C_n(\Delta x, \Delta y)$ of a single specimen, as defined by Eq. (24). For more details on calculating autocorrelation functions and performing ensemble averaging, see [27].

Once the correlation functions in Eqs. (27) and (28) have been computed, they can be fitted. However, only the autocorrelation function in the axial direction is fitted to ensure the smoothness of the realizations of the random fields. This is achieved by enforcing a zero slope at $\Delta x = 0$ in the autocorrelation function [26,54,55]. As the cylinder forms a closed structure, this condition is already satisfied for the autocorrelation function in the circumferential direction, calculated using Eq. (26). The locations at $\Delta y = 0$ and $\Delta y = 2\pi R$ are coincident, leading to a correlation of one and a zero slope in the autocorrelation function [22]. Therefore, only the axial autocorrelation function is approximated using a squared exponential function

$$\bar{\rho}_n(\Delta x, \ell_c) = \exp\left(-\frac{\Delta x^2}{\ell_c^2}\right), \tag{29}$$

where ℓ_c is the correlation length. The fitting is performed using the Non-linear Least Squares method [56]

$$\min_{\ell_c} \left[\frac{1}{2} \sum_{j=1}^{N_x} (z_i - \bar{\rho}_n(\Delta x_i, \ell_c))^2 \right], \tag{30}$$

where the correlation length ℓ_c is obtained as the fitting parameter.

As already proposed for the variance models in Eq. (23), when multiple shell specimens are available per batch, the mean autocorrelation function of all specimens in the batch,

$$\bar{C}(\Delta x, \Delta y) = \frac{1}{N_{\text{spec}}} \sum_{n=1}^{N_{\text{spec}}} C_n(\Delta x, \Delta y), \tag{31}$$

is used for the stochastic analysis.

Based on the measured imperfection data described in Section 2, the correlation model is evaluated for the lab- and full-scale suction buckets. The estimated axial and circumferential autocorrelation functions calculated by Eqs. (27) and (28) labeled as "measured" and their corresponding fits labeled as "fitted" for the full-scale and lab-scale suction buckets are shown in Figs. 6 and 7, respectively. For the two lab-scale suction buckets, the mean of the estimated correlation functions labeled as "measured-mean" and its fit labeled as "fitted-mean" are depicted in Fig. 7. These functions are finally used to

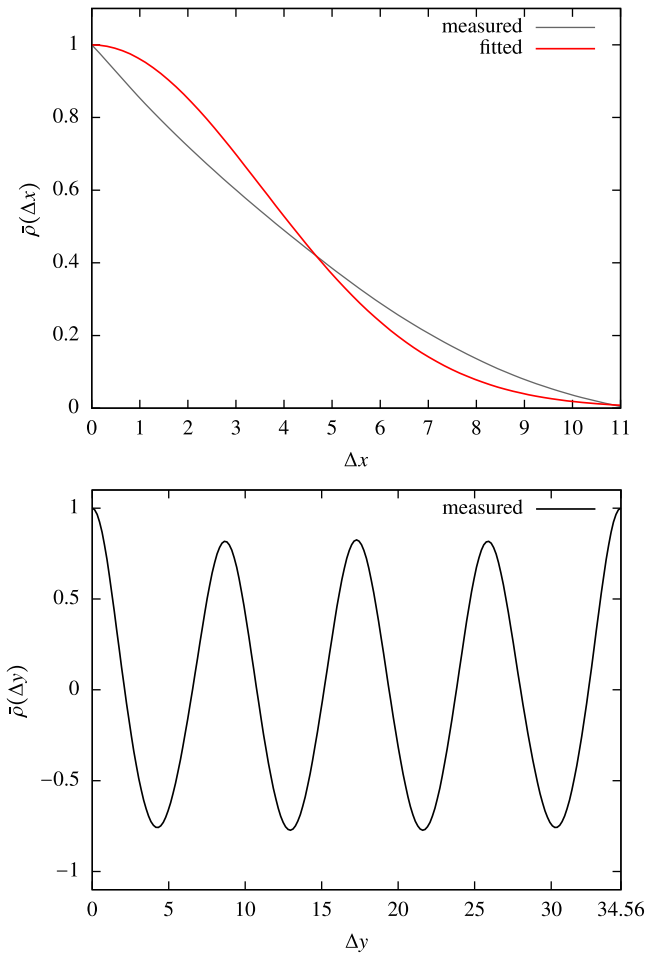

Fig. 6. Axial (top) and circumferential (bottom) autocorrelation functions of the full-scale suction bucket.

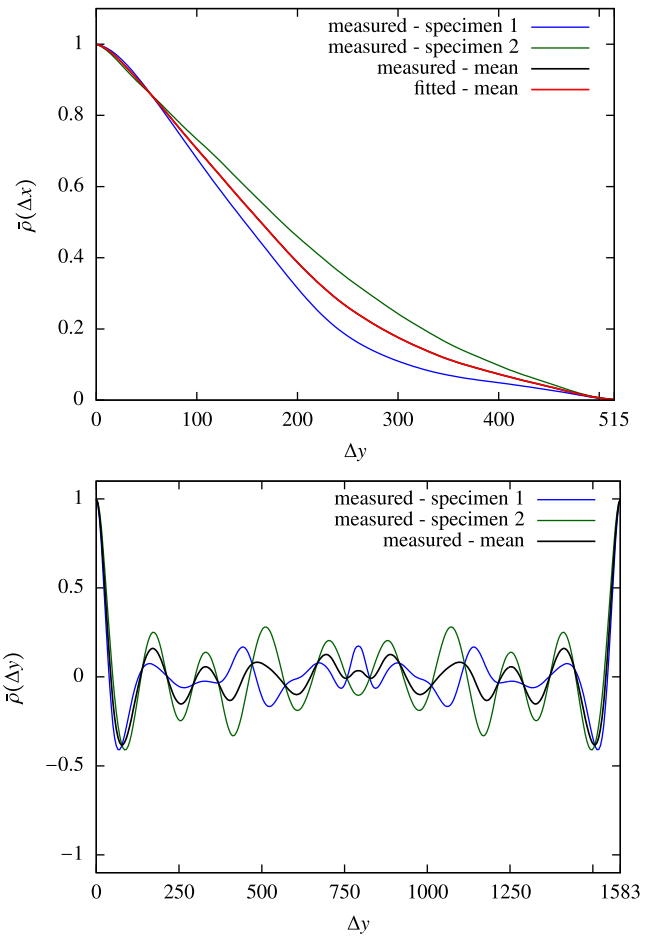

Fig. 7. Axial (top) and circumferential (bottom) autocorrelation functions of the lab-scale suction buckets.

generate the random imperfections in Section 5. The fitting yields an axial correlation length of $\ell_c = 5.0\,\text{m}$ for the full-scale suction bucket and $\ell_c = 207.5\,\text{mm}$ for the lab-scale suction buckets. Both fitted axial correlation functions are compared in Figs. 6 (top) and 7 (top). The correlation function of the full-scale shells shows a less steep drop from $\Delta x = 0$. As a result, the correlation is higher at small distances, indicating increased smoothness of the imperfection fields in the axial direction. The circumferential functions shown in Figs. 6 (bottom) and 7 (bottom) exhibit different wave numbers and amplitudes. However, all of these functions are symmetric with respect to the half-circumferential axis, since the circumferential distance is always defined as the shorter path around the cylinder, given by

$$\Delta y = \min \begin{cases} |y_i - y_j| \\ 2\pi R - |y_i - y_j|. \end{cases} \tag{32}$$

It can also be observed that the slope is zero at $\Delta y = 0$ and $\Delta y = 2\pi$, which satisfies the condition for smooth random imperfections.

4. Numerical models: validation & verification

Suction buckets for offshore wind turbines consist of a cylindrical shell (i.e., the skirt) and a lid. During the operational life, most of the skirt of the bucket is embedded in the seabed. For installation, water is pumped out from inside, creating a pressure difference within the foundation that forces the suction bucket into the seabed. This method allows for installation with low noise emissions and thus minimal environmental impact. A schematic sketch of a suction bucket installation is shown in Fig. 8, adapted from [22]. The suction bucket design, especially the skirt thickness, is primarily driven by the installation load case. During installation, the negative pressure acting on the skirt and the lid can cause shell buckling, which has to be considered in the design to ensure a safe foundation for the turbine tower.

In the following, the FE models for the lab-scale and a full-scale bucket, considering its surrounding soil, are introduced. FE buckling analyses require numerous modeling choices and represent a particular challenge [46]. These include selecting suitable shell elements with moderate or finite rotations, choosing path-following methods that can robustly capture highly non-linear behavior, defining reliable criteria to identify a stability point (e.g., eigenvalue problems, the determinant or negative diagonal elements of the tangent stiffness matrix), and accounting for the various possibilities of imperfection modeling, among others. Therefore, the FE models are compared with different FE programs from academia and industry, FEAP and ABAQUS, respectively. In a first step, the fundamentals of linear and non-linear buckling analysis are outlined. Subsequently, the numerical models of the suction buckets are verified and validated. The model of the lab-scale suction bucket with applied measured imperfections is validated through the pressures and displacements from the experiments. While, the FE model of the full-scale suction bucket is verified by comparing buckling pressures obtained for various boundary condition cases with the analytical solution.

4.1. Basics of linear and non-linear buckling analysis

Buckling analyses can be distinguished into linear and non-linear analysis. A linear bifurcation analysis (LBA) aims to identify stability

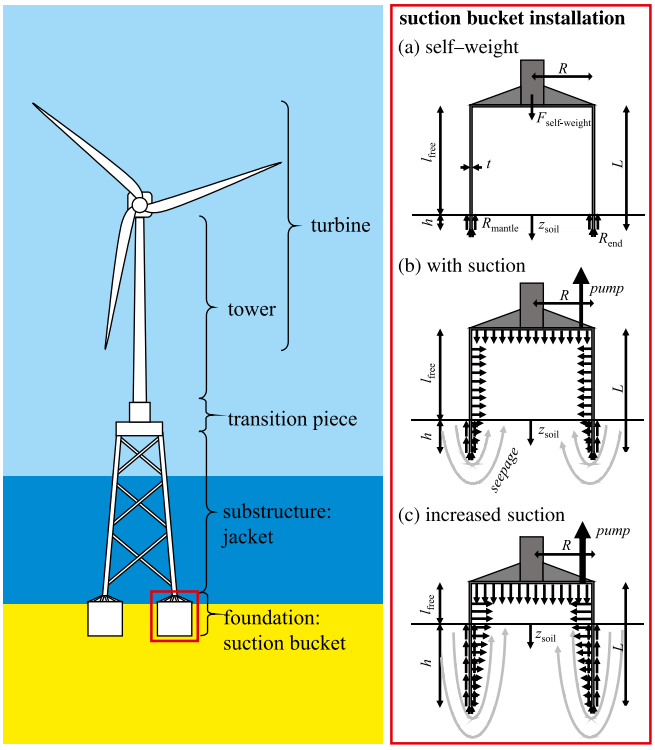

Fig. 8. Schematic sketch of suction bucket foundations for offshore wind turbines (left) and their installation (right).

points in the form of bifurcation points for structures with linear pre-buckling behavior. However, real-world structures frequently exhibit non-linear pre-buckling behavior due to material and geometrical non-linearities. Then, non-linear analyses are required, in which bifurcation and limit points are determined using iterative procedures such as the Newton–Raphson method, and for strongly non-linear problems, path-following algorithms such as the arc-length method are additionally employed.

Various numerical strategies are available to identify a stability point, as discussed, e.g., in [57,58]. In order to solve the LBA, a linear pre-buckling behavior is assumed. The LBA is based on the decomposition of the tangent stiffness matrix, which is divided into a linear part $\boldsymbol{K}_{\text{lin}}$ and a non-linear part $\boldsymbol{K}_{\text{nlin}}$, as

$$\begin{aligned}\boldsymbol{K}_T &= \boldsymbol{K}_{\text{lin}} + \boldsymbol{K}_{\text{nlin}} \\ &= \boldsymbol{K}_{\text{lin}} + \boldsymbol{K}_U(\boldsymbol{u}) + \boldsymbol{K}_G(\boldsymbol{\sigma}(\boldsymbol{u})).\end{aligned} \tag{33}$$

If the variational formulation allows separating $\boldsymbol{K}_{\text{nlin}}$, the initial displacement matrix $\boldsymbol{K}_U$ and the geometrical matrix $\boldsymbol{K}_G$ can be introduced.

In general, the tangent stiffness matrix depends on the displacement $\boldsymbol{u}$ and the associated stress state $\boldsymbol{\sigma}(\boldsymbol{u})$. However, the LBA is initialized with the displacement state $\boldsymbol{u} = \boldsymbol{0}$, where the linear solution

$$\boldsymbol{K}_T(\boldsymbol{0})\boldsymbol{u}_0 = \boldsymbol{P}_0 \quad \Leftrightarrow \quad \boldsymbol{u}_0 = \boldsymbol{K}_T^{-1}(\boldsymbol{0})\boldsymbol{P}_0 \tag{34}$$

is calculated for an external load $\boldsymbol{P}_0$ with $\boldsymbol{K}_T(\boldsymbol{0}) = \boldsymbol{K}_{\text{lin}}$. Consequently, the eigenvalue problem for a linear buckling analysis can be formulated as

$$[\boldsymbol{K}_{\text{lin}} + \Lambda \boldsymbol{K}_{\text{nlin}}]\,\boldsymbol{\varphi} = \boldsymbol{0}, \tag{35}$$

where the lowest eigenvalue Λ is used to increase the non-linear parts of the stiffness matrix. A stability point is indicated for $\Lambda = 1$. The associated eigenvector $\boldsymbol{\varphi}$ is an initial post-buckling mode. For $\Lambda = 1$,

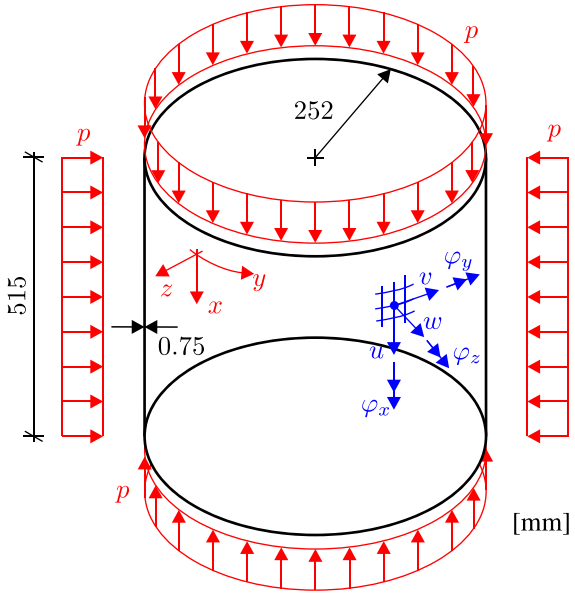

Fig. 9. FE model of the lab-scale suction bucket (unit: mm)

the mathematical expression for the stability eigenvalue emerges

$$\begin{aligned}(\boldsymbol{K}_{\text{lin}} + \Lambda_{\text{cr}}\boldsymbol{K}_{\text{nlin}})\boldsymbol{\varphi} = \boldsymbol{0} &\Leftrightarrow \boldsymbol{K}_T\boldsymbol{\varphi} = \boldsymbol{0} \\ &\Leftrightarrow (\boldsymbol{K}_T - \omega\boldsymbol{1})\boldsymbol{\varphi} = \boldsymbol{0},\end{aligned} \tag{36}$$

where a stability point is defined by $\omega = 0$. In the case of linear pre-buckling behavior, the assumption

$$\boldsymbol{P}_{\text{cr}} \sim \Lambda \boldsymbol{K}_{\text{nlin}} \tag{37}$$

leads to the calculation of the critical load

$$\boldsymbol{P}_{\text{cr}} = \Lambda \boldsymbol{P}_0, \tag{38}$$

and the corresponding critical displacement

$$\boldsymbol{u}_{\text{cr}} = \Lambda \boldsymbol{u}_0, \tag{39}$$

where the eigenvalue Λ is a load factor. In case of non-linear pre-buckling behavior, the results of a LBA may significantly deviate from the correct buckling load. This requires a non-linear buckling analysis, which involves a comprehensive non-linear path tracking analysis using an iterative procedure, such as the Newton–Raphson scheme. In this contribution, the non-linear buckling analysis is performed by a path-following analysis, where the signs of the diagonal elements of the tangent stiffness matrix $\boldsymbol{K}_T$ are observed. A reliable criterion to identify a stability point is the change in the sign of the diagonal elements, which also indicates a change in the equilibrium states

$$\begin{aligned}&\forall D_{ii} \quad , \quad D_{ii} > 0 \quad \rightarrow \quad \text{stable} \\ &\exists D_{ii} \quad , \quad D_{ii} = 0 \quad \rightarrow \quad \text{indifferent, (stability point)} \\ &\exists D_{ii} \quad , \quad D_{ii} < 0 \quad \rightarrow \quad \text{unstable.}\end{aligned} \tag{40}$$

If at least one of the diagonal elements D_{ii} becomes negative, the calculation is terminated, and the non-linear buckling load $P_{\text{cr,nlin}}$ is stored from the associated load vector $\boldsymbol{P}_{\text{cr,nlin}}$.

4.2. Finite element model of the lab-scale suction bucket

FE models are developed to analyze the buckling behavior of two lab-scale specimens. The results are validated with the experimental data. Fig. 9 shows the FE model with its dimensions and the applied pressure load. As described in Section 2, the shell length is 506 mm, and end plates with a thickness of 9 mm and a diameter of 504 mm

Table 2
Measured stress–strain values of the lab-scale shells converted into a quadlinear isotropic elasto-plastic material model.

Stress S [MPa]	119	148.75	171.45	345
Plastic strain E_p [%]	0	0.13605	0.65	25.4

are welded to the top and bottom. Taking into account the center-of-gravity line of the end plates, both specimens are modeled with a radius of $R = 252\,\text{mm}$, a length of $L = 515\,\text{mm}$, and a wall thickness of $t = 0.75\,\text{mm}$. The geometric imperfections of the two specimens, referred to as "specimen 1" and "specimen 2" are derived from the Fourier series described in Section 2. The corresponding Fourier coefficients are provided in the data repository at https://doi.org/10.25835/jn1a6pxa. For deterministic buckling analyses, no further scaling is applied after generating the imperfections using the Fourier series with the provided Fourier coefficients. Using the measured imperfection amplitudes allows to validate the simulated buckling pressures against the experimental results. The imperfections are modeled as geometric deviations in the radial direction (w) of the shell. In the FE model, the nodal coordinates $\boldsymbol{x}$ are modified in a stress-free manner as

$$\boldsymbol{x} = \boldsymbol{x} + \hat{w}(\boldsymbol{x}), \tag{41}$$

where the imperfection field $\hat{w}(\boldsymbol{x})$ can be represented either as a Fourier series according to Eq. (1) or as a random field according to Eq. (17).

In the following, ABAQUS and FEAP models are constructed. The ABAQUS model includes end plates and employs an isotropic elasto-plastic material model, whereas the FEAP model replaces the end plates with boundary conditions and uses an elastoplastic material model with exponential hardening. This is intended to show different modeling approaches yielding similar results to ensure a reliable probabilistic analysis subsequently.

4.2.1. ABAQUS model of the lab-scale shell

The ABAQUS model is generated with version 2019 [59], using shell elements with reduced integration (S4R). Following a convergence study considering the buckling pressures reported in [22], 314 elements in the circumferential direction and 103 elements in the axial direction are used for both FE models. In addition, care is taken to ensure that the imperfection pattern can also be represented adequately by the FE mesh. Furthermore, three Gaussian integration points through the shell thickness are used to capture possible non-linear stress distributions caused by plasticity effects. For the non-linear buckling analysis, the path-following Riks method (load-controlled) is applied. Both end plates with a thickness of 9 mm are fully discretized with an element edge length of 5 mm. The hydrostatic pressure is applied as an area load p on the mantle of the cylindrical shell and on the end plates. On the entire surface of the end plate at the bottom, the boundary conditions are $u = v = w = 0$. Whereas, no boundary conditions are set for the end plate at the top. The material of the specimens is deep-drawing steel DC 04. The Young's modulus is $E = 200\,\text{GPa}$ and the Poisson's ratio is $\nu = 0.3$. However, in contrast to structural steel, the yield point is not pronounced. An isotropic elasto-plastic material model is used, resulting in the stress–strain values given in Table 2. The stress values correspond to engineering stresses from tensile testing. These discrete points are used to define the piecewise linear hardening curve of the isotropic elasto-plastic material model.

4.2.2. FEAP model of the lab-scale shell

The ABAQUS shell model is compared with a FE model constructed using the FE program FEAP [60]. In the FEAP model, an isoparametric quadrilateral shell element based on Reissner–Mindlin theory and a three-field variational formulation is used. It is originally published in [61] and has been extended in [62] by independent thickness strains in order to allow for arbitrary 3D constitutive equations. The present version [63] is additionally capable of calculating the stress state in layered structures with different materials. The shell element formulation allows for the selection of either moderate or finite rotations to consider geometrically non-linear behavior. For all investigations presented in this study, moderate rotations are used. As in the ABAQUS model, following a convergence study, 314 elements in the circumferential direction and 103 elements in the axial direction are used. Furthermore, four Gaussian integration points through the shell thickness are used to capture possible non-linear stress distributions caused by plasticity effects. In contrast to the ABAQUS model, the welded end plates are replaced by boundary conditions simulating clamped edges. This means that at the bottom and top edges, all rotations are fixed: $\varphi_x = \varphi_y = \varphi_z = 0$. The displacement boundary conditions at the bottom are $u = v = w = 0$ and at the top $v = w = 0$, where the degree of freedom in the u-direction must remain free due to the applied pressure load, see Fig. 9. The circumference pressure is defined as an element load p. The area loads p on the end plates, which are replaced by the clamped boundary conditions, are simulated by equivalent edge loads $p_e = p\pi R^2/2\pi R = pR/2$. The equivalent load at the bottom edge is neglected due to the boundary conditions in the u-direction. To evaluate the buckling load and the load–displacement curves with FEAP, the cylinder is subjected to incremental loading with a step size of $\Delta p = 1$ kPa, which is reduced to $\Delta p = 0.1\,\text{kPa}$ close to the stability point. In the non-linear analysis, the critical buckling load $p_{\text{cr,nlin}}$ is determined as the load level at which the first zero diagonal entry D_{ii} appears in the tangent stiffness matrix. The non-linear problem is solved using the Newton–Raphson method.

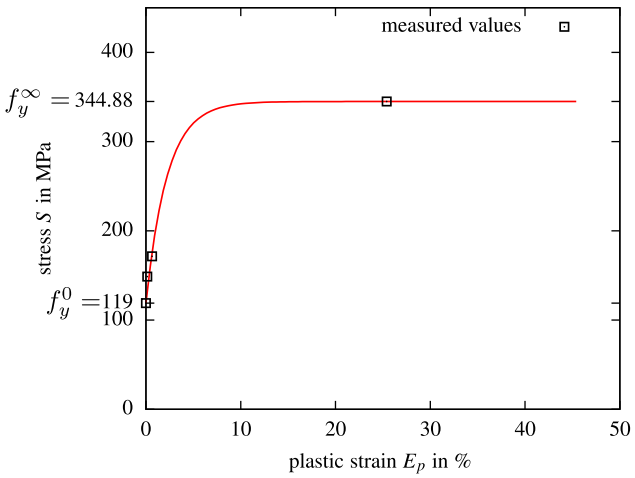

Fig. 10. Fitted stress–strain curve for elasto-plastic material model of the lab-scale shells with exponential hardening provided in FEAP.

The elasto-plastic material model with exponential hardening is used. The corresponding stress function is defined as

$$S = f_y^0 + (f_y^\infty - f_y^0)\left[1 - e^{-x_d E_p}\right], \tag{42}$$

where E_p is the plastic strain, f_y^0 is the initial yield stress, f_y^∞ is the yield stress at $E_p = \infty$, and x_d is the exponential hardening parameter. A parameter fitting is conducted using the measured stress–strain values given in Table 2. The initial yield stress is set to $f_y^0 = 119\,\text{MPa}$, and a Non-linear Least Squares fitting yields $f_y^\infty = 344.88\,\text{MPa}$ and $x_d = 44.54$. The corresponding fitted stress–strain curve is depicted in Fig. 10.

4.2.3. Comparison and validation of the lab-scale shell models

The ABAQUS and FEAP models for the lab-scale suction bucket are shown in Fig. 11. The measured geometric imperfections of "specimen 1" and "specimen 2" of the lab-scale shells, shown in Figs. 2 and 3, are applied to the ABAQUS and FEAP models. Both models are

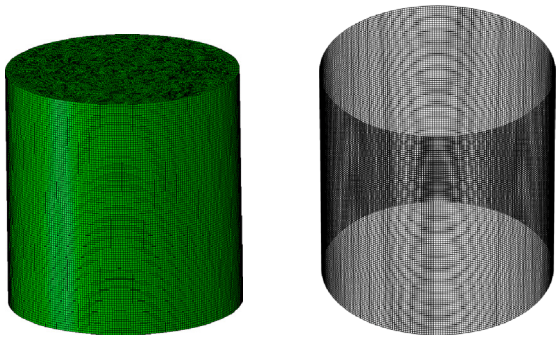

(a) ABAQUS (b) FEAP

Fig. 11. FE models for the lab-scale suction bucket.

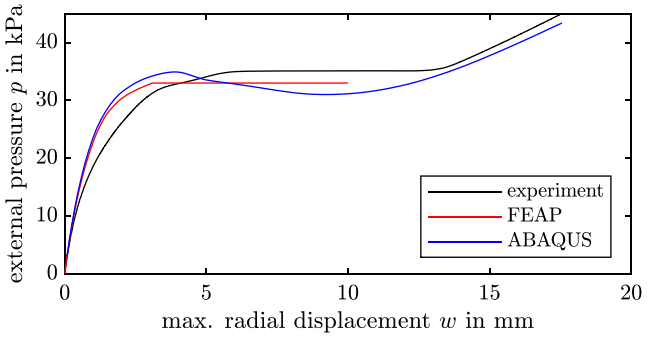

Fig. 12. Load–displacement curves of specimen 1.

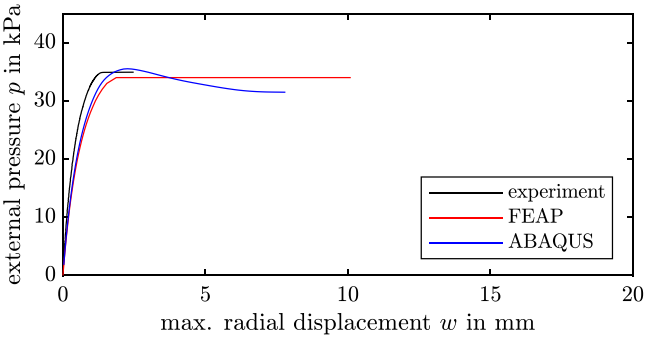

Fig. 13. Load–displacement curves of specimen 2.

validated using the experimentally measured load–displacement curves of the two specimens, see Figs. 12 and 13 for specimens 1 and 2, respectively. Overall, for both specimens, a close agreement between the numerical and experimental results can be observed, particularly in the buckling pressure. The experimental curve of specimen 1 in Fig. 12 exhibits a noticeably softer pre-buckling response. However, the FEAP and ABAQUS curves of both specimens are closely aligned. This is confirmed by the computed eigenvectors from the linear buckling analysis. In the FEAP and ABAQUS models, 9 full waves and 18 half waves can be identified in the first eigenmodes, see Fig. 14.

Finally, the experimental and numerical results of the buckling pressures are summarized in Table 3. The GMNIA is performed using the measured geometric imperfections of specimens 1 and 2 applied to the ABAQUS and FEAP models. Only minor deviations are observed between the GMNIA results obtained with FEAP and ABAQUS. However, a noticeable discrepancy of approximately $1 - 55.2/61.2 = 10\,\%$ between the FEAP-LBA and ABAQUS-LBA results is shown in Table 3. In ABAQUS, the Lanczos eigenvalue solver is employed, whereas the FEAP-LBA analysis is performed using the subspace eigenvalue solver. The different eigenvalue solution methods can contribute to the observed discrepancy. However, the different lid modeling approaches are expected to have a larger influence on the LBA results than on the GMNIA results.

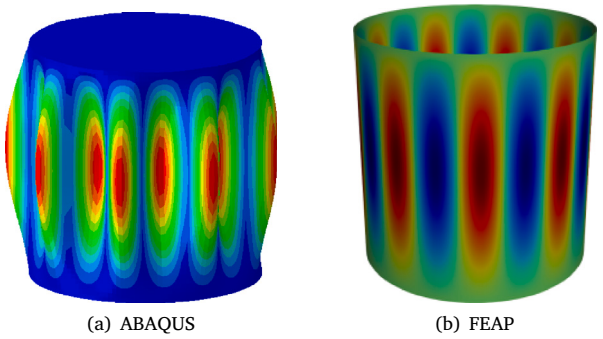

(a) ABAQUS (b) FEAP

Fig. 14. First eigenmodes of the lab-scale shell model.

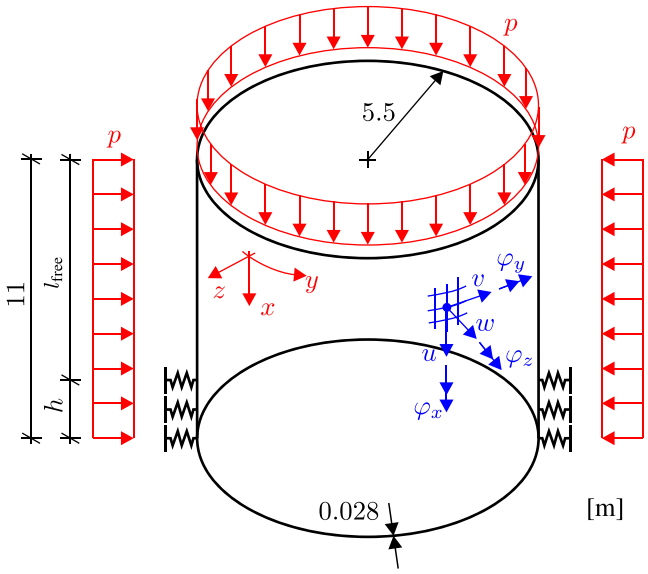

Fig. 15. FE model of the full-scale suction bucket (unit: m).

4.3. Finite element model of the full-scale suction bucket

The proposed random field approaches presented in Section 3.2 are applied to a full-scale suction bucket. Dimensions of the suction bucket are designed to represent those of 10 MW turbines, such as those used in the seagreen wind farm [64]. The design described in [65] is applied, where the skirt has a radius of $R = 5.5$ m, a length of $L = 11$ m and a thickness of $t = 0.028$ m. The geometry, loads, degrees of freedom, and coordinate system of the full-scale suction bucket model are depicted in Fig. 15. The total length of the shell L is divided into the free length l_{free} and an embedment depth h. The suction bucket already sinks into the soil under its self-weight, i.e., the embedded case $h = 0$ is not relevant in practice. Therefore, the probabilistic analysis in Section 5.3 focuses on the embedded case ($h > 0$), which is performed using the ABAQUS model. In this model, a soil model based on non-linear soil springs proposed in [22] is implemented. The full-scale shell has a lid and is open at the bottom. Further details of the lid design can be found in [22]. The geometric imperfections derived from the Fourier series

Table 3
Experimental and numerical results of the buckling pressures in [kPa] of the two specimens of the lab-scale shells.

	experiment	LBA-ABAQUS	LBA-FEAP	GMNIA-ABAQUS	GMNIA-FEAP
specimen 1	35.1	61.2	55.2	35.0	33.0
specimen 2	34.9	61.2	55.2	35.5	34.0

described in Section 2 are applied as stress-free out-of-plane deviations of the shell in the w-direction. The nodal coordinates are modified as defined in Eq (41). The corresponding Fourier coefficients are provided in the data repository at https://doi.org/10.25835/jn1a6pxa. Since the geometry of the investigated full-scale suction bucket differs from that in [45], from which the measured imperfections are taken, and in order to investigate a worst-case scenario, the measured imperfections shown in Fig. 1 are scaled before calculating the Fourier coefficients to a maximum peak-to-peak value of 119.5 mm to match fabrication tolerance class C according to [2]. Therefore, for the deterministic buckling analysis, no further scaling is applied after generating the imperfections using the Fourier series with the provided Fourier coefficients.

4.3.1. Analytical solution

As a preliminary step, the unembedded case ($h = 0$) of the ABAQUS model is compared to an FE model in FEAP, and the solutions of the linear buckling analyses are verified with an analytical solution. The analytical ideal elastic solution of a cylindrical shell under external pressure, which is derived from [66], is defined as

$$p_{\mathrm{cr,ref}} = \frac{Et^2}{R^2}\left[\frac{\sqrt{2}}{3\sqrt{3}}\frac{\pi}{(1-\nu^2)^{0.75}}\frac{R}{L}\sqrt{\frac{t}{R}}\right]. \tag{43}$$

For a Poisson's ratio of $\nu = 0.3$ the equation simplifies to

$$p_{\mathrm{cr,ref}} = 0.918\,\frac{Et^2}{RL}\sqrt{\frac{t}{R}} = 178\,\mathrm{kPa}. \tag{44}$$

This correlates to the rearranged form of the equation provided in Eurocode 3 [2]. In this analytical solution, only a uniformly distributed external pressure on the mantle of the cylindrical shell is considered, with no simultaneously acting axial pressure. The cylindrical shell is simply supported, allowing a displacement in the axial direction (u). Thus, the boundary conditions are similar to $v = w = 0$ at both the bottom and top edges. It should be noted that the analytical buckling pressure in Eq. (44) corresponds to elastic shells without any imperfections and to the defined idealized boundary conditions. Thus, the numerical solution of the linear buckling analysis can be verified. Differences from the analytical solution indicate imperfection sensitivity and non-linear material behavior of cylindrical shells under external pressure.

4.3.2. ABAQUS model of the full-scale shell

As for the lab-scale shell, the ABAQUS model is generated with version 2019 [59], using shell elements with reduced integration (S4R). The non-linear buckling analysis is performed using the path-following Riks method (load-controlled). Based on a convergence study, the skirt mesh is refined to 216 elements along the circumference and 69 elements along the axial direction, and three Gaussian integration points through the shell thickness are used to capture possible non-linear stress distributions caused by plasticity effects. In addition, it is ensured that the imperfection pattern can also be represented adequately by the FE mesh. Two configurations are modeled for the unembedded case: with and without a lid, where the buckling behavior for different boundary conditions is analyzed in Section 4.3.4. The lid is modeled as S4 shell elements rigidly connected to the skirt, providing some rotational restraint compared to pinned boundary conditions; the detailed geometry is given in [22]. A quad-linear stress–strain model according to [67] is used. The corresponding material parameters for structural steel S355, namely Young's modulus E, Poisson's ratio ν, yield stress f_y, and ultimate tensile strength f_u, are given in Table 4.

Table 4
Material properties of the full-scale suction bucket using the structural steel S355.

E [MPa]	ν [–]	f_y [MPa]	f_u [MPa]
210000	0.3	355	490

Investigations for different embedment depths ($h > 0$) are presented in Section 5.3. For this purpose, the shell with the lid is extended by a soil model at the bottom. In the vertical direction (u), the suction bucket model is fixed at the bottom edge. The soil is modeled using non-linear soil springs to reduce computation times. To each element of the shell, which is considered to be embedded in the soil, one non-linear spring is coupled in the radial direction (w). The springs are calibrated with a Mohr–Coulomb soil model, considering a Young's modulus of $E_{\mathrm{soil}} = 50$ MPa, which is commonly assumed to be equivalent to the reference secant modulus at 50 % strength E_{50}, a Poisson's ratio of $\nu_{\mathrm{soil}} = 0.28$, a friction angle of $\phi = 38°$, a dilatation angle of $\psi = 8°$, a relative density of $\rho = 1000\,\mathrm{kg/m^3}$ and a relative earth pressure coefficient of $K = 0.5$. Taking into account circumferential loading, the non-linear reaction force–displacement curves are extracted and fitted as described in [22], resulting in one non-linear soil spring equation per nodal layer.

4.3.3. FEAP model of the unembedded full-scale shell

To compare the results of the buckling analysis of the unembedded ABAQUS full-scale shell model, a model without the lid is constructed in FEAP. The same isoparametric quadrilateral shell elements, based on the Reissner–Mindlin theory and a three-field variational formulation, are used as in the lab-scale suction bucket model described in Section 4.2.2. Moderate rotations are selected in the geometrically non-linear formulation. As in the ABAQUS model, 216 elements along the circumference and 69 elements along the axial direction are used based on a convergence study. In addition, four Gaussian integration points through the shell thickness are defined to model possible non-linear stress distributions caused by plasticity effects. For the verification with the analytical solution, different boundary conditions are discussed in Section 4.3.4.

An elasto-plastic material model is used, with an initial yield stress $Y_0 = f_y$ set to 355 MPa and a linear hardening factor of $c_p = E/100$ as recommended in [68]. The circumference pressure p is defined on the element level. In the non-linear analysis, the cylinder is loaded with a step size of $\Delta p = 10$ kPa which is reduced to $\Delta p = 1$ kPa near the stability point. The buckling load $p_{\mathrm{cr,nlin}}$ is identified when the first zero diagonal element D_{ii} occurs in the tangent stiffness matrix. The non-linear analysis is performed using the Newton–Raphson scheme.

4.3.4. Comparison and verification of the unembedded full-scale shell models

Both FE models of the full-scale suction bucket, the ABAQUS model including the lid and the FEAP model without a modeled lid, are shown in Fig. 16. The solutions of the linear buckling analysis (LBA), the geometrically and materially non-linear analysis with imperfections (GMNIA) and the corresponding critical buckling load factor α_{cr} for four cases of boundary conditions are shown in Table 5. In this study, the critical buckling load factor α_{cr} is defined as

$$\alpha_{\mathrm{cr}} = \frac{p_{\mathrm{cr,nlin}}}{p_{\mathrm{cr}}}, \tag{45}$$

Table 5
Numerical results of the unembedded full-scale suction bucket for different boundary condition cases.

Case	Boundary conditions	Model	LBA p_{cr} [kPa]	GMNIA $p_{cr,nlin}$ [kPa]	α_{cr} [–]	$\epsilon_{ref.}$ [%]	$\epsilon_{mod.}$ [%]
1	bottom: $u = 0$ (one node), $v = w = 0$; top: $v = w = 0$	ABAQUS (w/o lid) FEAP (w/o lid)	187 190	152 149	0.81 0.78	4.8 6.3	3.7
2	bottom: $v = w = 0$; middle: $u = 0$; top: $v = w = 0$	FEAP (w/o lid)	190	152	0.80	6.3	–
3	bottom: $u = v = w = 0$; top: $v = w = 0$	ABAQUS (w/o lid) FEAP (w/o lid)	224 228	177 177	0.79 0.78	20.5 21.9	1.3
4	bottom: $u = v = w = 0$; top: lid	ABAQUS (with lid)	235	183	0.78	24.3	–

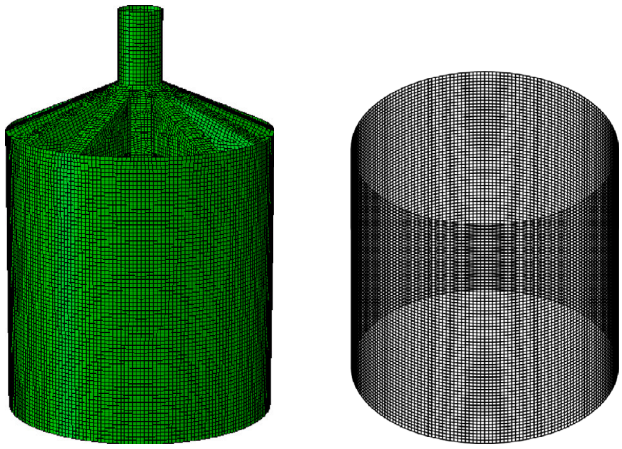

(a) ABAQUS model with lid (b) FEAP model without lid

Fig. 16. Finite element (FE) models of the full-scale suction buckets.

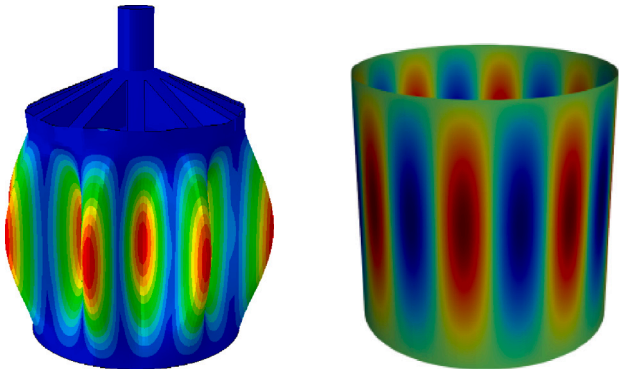

(a) ABAQUS model with lid (b) FEAP model without lid

Fig. 17. First eigenmodes of the full-scale shell models computed by ABAQUS and FEAP.

where p_{cr} denotes the buckling load obtained from the linear bifurcation analysis LBA of the cylinder without imperfections and material non-linearities, and $p_{cr,nlin}$ denotes the buckling load obtained by the non-linear buckling analysis as described in Section 4.1 considering geometric imperfections and material non-linearities (GMNIA). It should be emphasized that depending on the engineering discipline, the critical buckling load factor α_{cr} is often specified without taking into account material non-linearities, such as plasticity. In the analytical solution given in Eq. (44), the cylinder is assumed to be simply supported and the cylinder is free to deform in the axial direction (u). The boundary conditions are similar to $v = w = 0$ at the bottom and top edge. To avoid a kinematic FE model, the cylinder has to be fixed in the axial direction (u). Therefore, only one node at the bottom edge is fixed in the axial direction (u) in case 1 of Table 5. The hydrostatic pressure is considered by a circumferential compression p on the mantle of the shell, and, as in the analytical solution, no pressure is applied at the bottom and top edges in the axial direction. The analytical solution can be closely approximated by both FEAP and ABAQUS (w/o lid), with, for example, only a minor error of approximately $\epsilon_{ref.} = 1 - 178/190 = 6.3\,\%$ for the FEAP model. Alternatively, to ensure symmetry, the nodes around the middle of the cylinder can be fixed, as investigated with FEAP in case 2. To ensure that a row of nodes is in the middle for applying the boundary conditions, the number of elements in the axial direction is increased by one to 70 elements (71 nodes) in this case. The buckling loads from LBA and GMNIA align with those of case 1 and the analytical solution. In case 3, the cylinder is simply supported, with the boundary conditions $u = v = w = 0$ at the bottom edge and $v = w = 0$ at the top edge. The pinned boundary conditions at the top $v = w = 0$ are intended to conservatively simulate the replaced lid. The boundary conditions at the bottom $u = v = w = 0$ are selected due to the fact that the suction bucket sinks already into the soil under its self-weight. A fully unembedded case ($h = 0$), where the suction bucket can deform freely, is not realistic. Therefore, the radial and axial displacements are assumed to be fixed ($u = 0$ and $w = 0$) at the bottom edge. However, the solutions of case 3 disagree with the analytical buckling load in Eq. (44) by, for example, approximately $\epsilon_{ref.} = 1 - 178/228 = 21.9\,\%$ for the FEAP model. These boundary conditions lead to a higher critical buckling pressure. In case 4, the ABAQUS model incorporates the lid. The boundary conditions at the bottom edge are $u = v = w = 0$, while no boundary conditions are applied at the top due to the lid. In addition to the circumferential compression p on the skirt, the pressure on the lid is directly imposed as an area load p. The solution matches closely the buckling pressures obtained by LBA and GMNIA of case 3 without the lid. In cases 1 and 3, the solutions for the critical buckling load factors show close agreement between ABAQUS and FEAP, with a small error of $\epsilon_{mod.}$ of 1.3 %–3.7 %. However, the results highlight the sensitivity of the numerical results to the boundary conditions. For this reason, the models are compared using FEAP and ABAQUS and verified with an analytical solution before performing the comprehensive probabilistic analysis in the following Section 5.

Finally, the first eigenmodes of both models, ABAQUS and FEAP are shown in Fig. 17. In the design of steel shells, these eigenmodes are commonly used as equivalent geometric imperfection forms for non-linear analyses. The load–displacement curves of the different modeling approaches for the non-linear buckling analysis (GMNIA) and boundary conditions case 1 and 4 according to Table 5 are compared in Fig. 18. For this purpose, the maximal radial displacement w is presented. The load–displacement curves from FEAP and ABAQUS without the lid show differences in initial stiffness, but agree in terms of the peak load. The curve of the ABAQUS bucket with the fully discretized lid at the top exhibits a stiffer behavior.

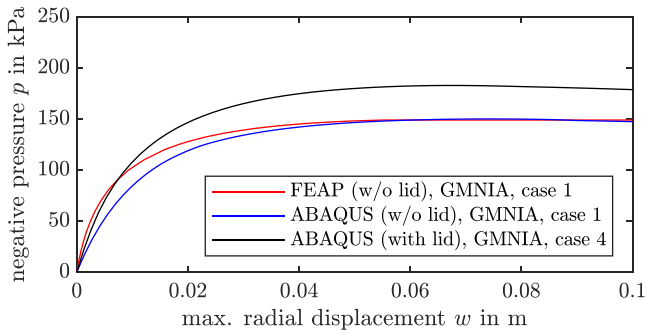

Fig. 18. Load–displacement curves for the non-linear buckling analysis (GMNIA) of the full-scale suction bucket model for the boundary conditions case 1 (FEAP and ABAQUS (w/o lid)) and case 4 (ABAQUS (with lid))

5. Probabilistic buckling analysis

The influence of non-homogeneity on the second-order statistics (mean and variance) of the buckling load is evaluated by performing Monte Carlo simulations. Random geometric imperfections are generated from the three variance approaches in Section 3 and applied to the models described in Section 4. The results are compared to experimental and design loads. For the full-scale suction bucket model, different embedment depths are investigated, considering various non-linear spring sets. The results of the Monte Carlo Simulation (MCS) are based on 500 realizations.

5.1. Samples of random geometric imperfections

Random imperfections are generated based on the proposed variance approaches and the correlation model using the Karhunen–Loève expansion given in Eq. (17). As recommended in Section 3, the series is truncated to retain 99 % of the total sum of eigenvalues. Furthermore, all generate samples of random imperfections are scaled to a maximum imperfection amplitude $\Delta\hat{w}_s$ by

$$\hat{w}_s(\boldsymbol{x},\theta) = \Delta\hat{w}_s \cdot \frac{\hat{w}(\boldsymbol{x},\theta)}{|\max(\hat{w}(\boldsymbol{x},\theta))| + |\min(\hat{w}(\boldsymbol{x},\theta))|}. \tag{46}$$

The samples of the full-scale suction bucket are scaled to $\Delta\hat{w}_s = 119.5\,\text{mm}$, which is the maximum amplitude according to the fabrication tolerance quality class FQC C defined in [2]. To ensure comparability with the Fourier-based approach, the samples of the lab-scale shells are scaled to an imperfection amplitude of $\Delta\hat{w}_s = 3.05\,\text{mm}$, which is the mean of the amplitudes of both measured Fourier imperfections.

In Figs. 19 and 20, the Fourier series of the measured imperfections and samples of random geometric imperfections for the full-scale and lab-scale suction buckets, calculated from the proposed variance models, are depicted. It can be observed that the measured imperfection of the full-scale suction bucket in Fig. 19 exhibits larger deviations from the reference shell geometry at the lower free edge and smaller deviations at the upper edge, which is welded to the lid. This indicates a characteristic non-homogeneous imperfection pattern, which may be attributed to the fabrication process. It is plausible that deviations at the welded connection to the lid are more controllable during manufacturing than those at the lower end of the cylindrical skirt. However, it is shown later in the paper that it is important to consider the non-homogeneity in the modeling of imperfections. In the samples generated using the homogeneous variance model ("hom"), it is evident that the non-homogeneity cannot be captured. All samples exhibit the same waviness at both the bottom and the top. In contrast, the variance models "non-hom 1" and "non-hom 2" produce imperfection patterns that are visually more realistic by capturing the non-homogeneity.

In Fig. 20, the Fourier series of the measured imperfections of the lab-scale shells captures both the weld depression imperfection and the two intentionally introduced dimples. These features will consistently appear in specimens produced using the same manufacturing process and identical post-fabrication treatment. However, the samples generated using the variance models "hom" and "non-hom 1" do not exhibit a single welded seam, but rather multiple imperfections similar to longitudinal weld depressions. This does not correspond to the measurements. However, the samples generated using the variance approach "non-hom 2" resemble the measured imperfections. As shown in Fig. 5 (right), this non-homogeneous variance model reduces the variance across large areas of the domain, leading to the desired imperfection pattern with a single welded seam.

Table 6
MCS results of the buckling pressure $p_{\text{cr,nlin.}}$ for the lab-scale suction bucket.

	min [kPa]	max [kPa]	mean [kPa]	CoV [%]
hom	26	42	32	9.1
non-hom 1	26	40	31	7.6
non-hom 2	28	48	37	9.8

5.2. Results of the lab-scale suction buckets

The proposed random field approaches are applied to the lab-scale suction buckets, and probabilistic buckling analyses are performed using the FEAP model described in Section 4.2.2. The results of the MCS for the three modeling approaches ("hom", "non-hom 1" and "non-hom 2") are shown in Fig. 21. The corresponding minimum, maximum, and mean values, as well as the coefficient of variation (CoV), are provided in Table 6. In Fig. 21, the large deviation of the results from the buckling load obtained with the linear bifurcation analysis without applied imperfections, labeled as LBA, can be seen. The largest mean buckling pressure and CoV result from the non-homogeneous approach "non-hom 2". The mean value obtained from this approach, $p_{\text{cr,nlin}} = 37.01\,\text{kPa}$, is also the closest to the mean value of the buckling loads from the experiments of the two specimens in Table 3, $p_{\text{cr,exp}} = 35\,\text{kPa}$, labeled as "experiment". In Fig. 20, it can be observed that the generated random imperfections using the "non-hom 2" approach resemble the measured imperfection pattern. Individual weld seams can be represented most accurately with this approach. Furthermore, the imperfections generated using the "hom" and "non-hom 1" approaches look very similar. This also explains the nearly identical results of the stochastic analysis with respect to the observed minimum, maximum, and mean buckling pressures. The "hom" and "non-hom 1" approaches yield the smallest mean buckling pressures. The reason is that, for the investigated load case under negative pressure, global imperfections are less favorable than local individual weld seams generated with the "non-hom 2" approach. It should be noted that, unlike the full-scale bucket, where the largest imperfections occur at the bottom and are nearly zero at the top, the non-homogeneity of the lab-scale shells is not strongly pronounced in the axial direction. However, the localized imperfections can be modeled by considering non-homogeneity in the circumferential direction. To verify these results, more specimens have to be tested.

5.3. Results of the full-scale suction bucket

The MCS of the full-scale suction bucket is performed using the ABAQUS model described in Section 4.3.2, where the soil model proposed in [22] is implemented. Fig. 22 shows the histograms of the different random field approaches for the full-scale suction bucket without the soil model. The results are compared with the buckling load obtained from the measured imperfection pattern approximated by a Fourier series and applied to the FE model, labeled as "measured", as well as with the linear bifurcation analysis without applied imperfections, labeled as "LBA". It can be observed that the random geometric imperfections generated with the homogeneous variance model

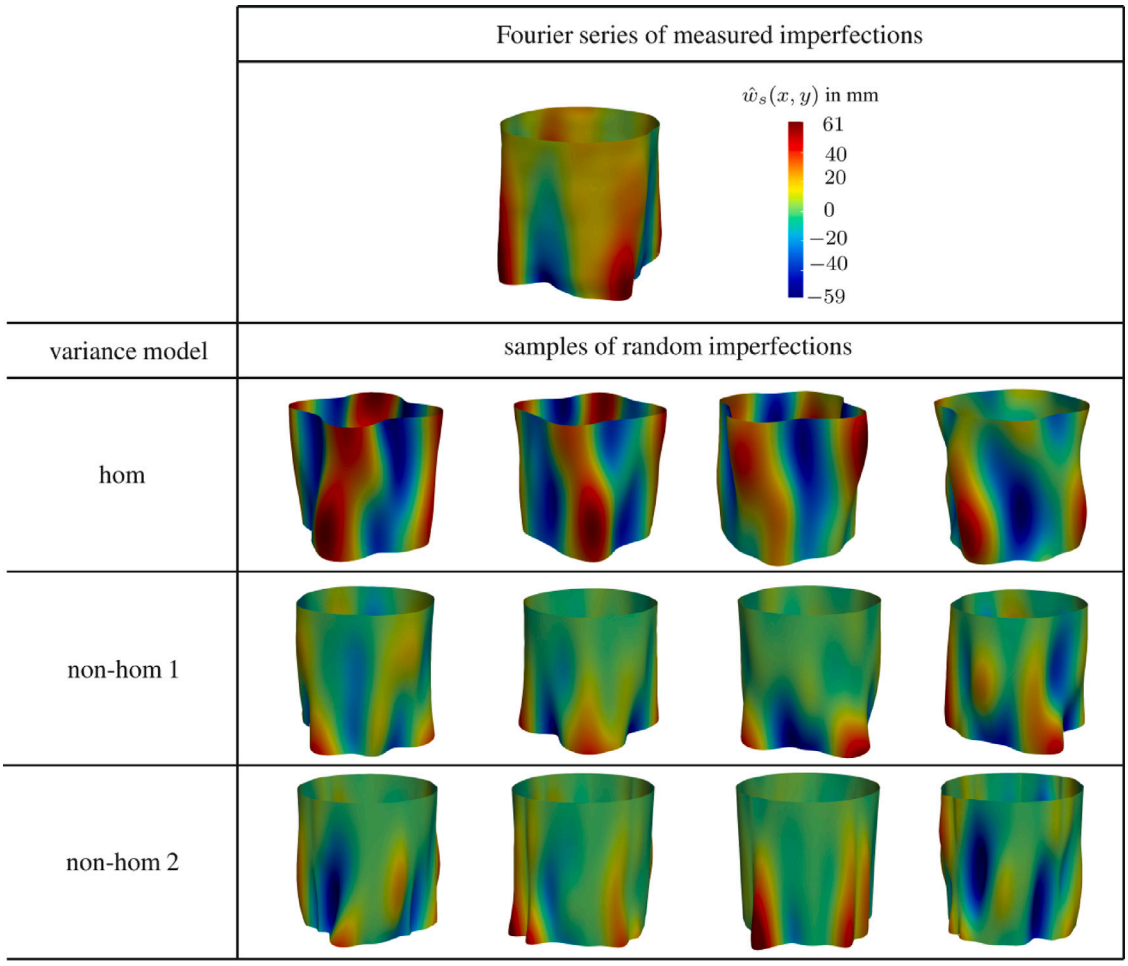

Fig. 19. Full-scale suction bucket: Fourier series of the measured imperfection and samples of random geometric imperfections generated using the proposed variance models (20× magnified).

"hom" result in the lowest mean buckling pressure. In this model, the geometric imperfection pattern, depicted in Fig. 19, shows the same waviness at the top and the bottom, and large dents can occur in the middle of the shell, which explains the largest reduction in the mean buckling pressure. The mean buckling pressures obtained from the MCS using the non-homogeneous variance models ("non-hom 1" and "non-hom 2") closely match the buckling pressure of the shell with the applied measured imperfection pattern. As discussed in Section 5.1, the measured characteristic of the non-homogeneous imperfection pattern of the full-scale bucket shows larger deviations at the bottom and, due to the welding of the lid, smaller geometric imperfections at the top, see Fig. 19. In other words, the imperfections are narrower or locally distributed. This can be accurately simulated using both non-homogeneous random field approaches. The more locally distributed imperfections are less unfavorable than global imperfections in this load case. This explains the higher mean buckling pressures compared to the MCS results, which are computed using the homogeneous random field approach that generates more global-like imperfections.

The results for the three modeling approaches ("hom", "non-hom 1", and "non-hom 2") with an embedment depth of 4 m, which is for this design a critical depth, are depicted in Fig. 23. The critical embedment depth depends on the soil properties. To prevent hydraulic failure during the installation process, critical suction has to be considered. As discussed in [22], for large embedment depths exceeding 7 m, where the free shell length is short, the buckling resistance is significantly higher than the critical suction. At small embedment depths, only moderate pumping is required to overcome the soil resistance, resulting in a low risk of buckling due to the limited negative pressure. The most critical phase occurs during the first half of the installation process. For the present design, the critical embedment depth is approximately 4 m, which aligns with values predicted by classical design approaches. As can be seen in Fig. 23, the difference between the mean buckling pressures obtained using the homogeneous model and the non-homogeneous approaches increases. Moreover, the variance increases for all approaches. When considering soil, the homogeneous approach "hom" results in the lowest buckling resistance, whereas the non-homogeneous approaches "non-hom 1" and "non-hom 2" lead to higher buckling resistance. The larger difference between the resulting pressures can be explained by the fact that the largest modeled waves are located at the bottom edge of the cylinder, which is embedded and thus partially restrained by the soil. Along the free shell length above the mudline, the non-homogeneous modeling approaches generate only small geometric imperfections. As shown previously in Fig. 22, the mean buckling pressures from the MCS using both non-homogeneous variance approaches closely agree with the numerical buckling load obtained with the applied measured Fourier imperfection pattern on the FE model, denoted as "measured". A summary of the MCS results, including the minimum, maximum, mean value, and coefficient of variation (CoV), for the full-scale suction bucket with different embedment depths is given in Table 7. The mean value and the CoV increase for higher embedment depths. However, the variance increases slightly and remains in a comparable range for all random

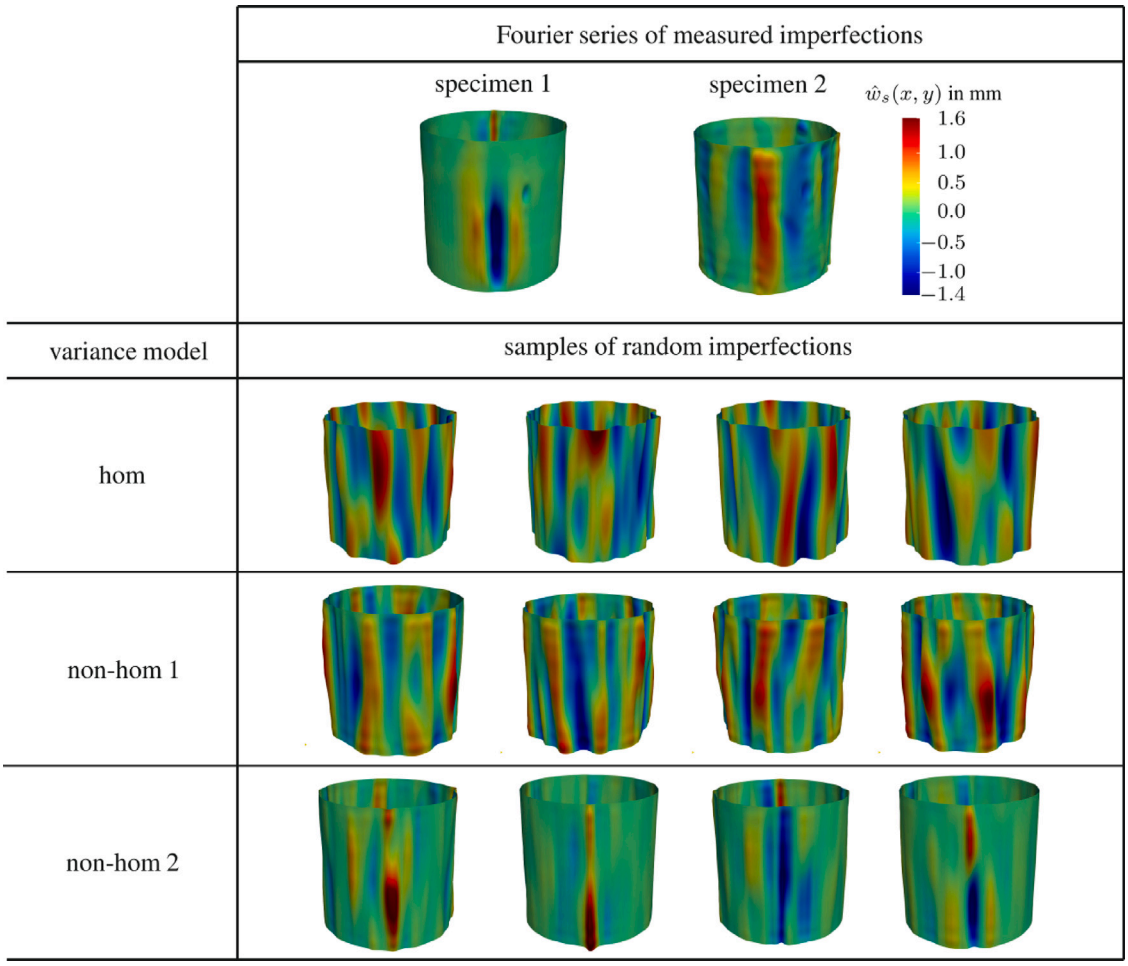

Fig. 20. Lab-scale suction buckets: Fourier series of the two measured imperfections and samples of random geometric imperfections generated using the proposed variance models (20× magnified).

Table 7
MCS results of the buckling pressure $p_{cr,nlin.}$ for the full-scale suction bucket with different embedment depths.

	hom				non-hom 1				non-hom 2			
depth h [m]	min [kPa]	max [kPa]	mean [kPa]	CoV [%]	min [kPa]	max [kPa]	mean [kPa]	CoV [%]	min [kPa]	max [kPa]	mean [kPa]	CoV [%]
1	92	185	138	11.0	85	206	149	11.3	115	207	155	11.3
2.5	115	215	166	10.5	135	235	188	10.2	142	230	187	10.4
4	120	241	182	11.3	149	267	213	10.5	155	257	209	10.9
5.5	129	291	204	12.3	167	318	248	11.5	172	307	240	12.0
7	152	356	253	12.9	217	420	325	10.7	213	388	305	12.2

field modeling approaches. It should be noted that Table 7 starts with an embedment depth of $h = 1$ m. This is due to the fact that the suction bucket sinks already into the soil under its self-weight. The unembedded case ($h = 0$) is therefore not practically relevant. Fig. 24 shows the empirical cumulative distribution functions (ecdf) of the full-scale suction bucket design with an embedment depth of 4 m, obtained using the proposed modeling approaches. A Gaussian distribution is fitted to the simulated ecdf. The fitted distributions are evaluated to yield quantiles that represent a target reliability level of 99.99 %, as recommended for most applications according to [69]. The results of the three random field modeling approaches are compared with classical approaches used in the design of steel structures according to EC3: stress design with reduction factors, GMNIA applying the 'worst' eigenmode as the imperfection form, and, as a reference, the linear bifurcation analysis. For shells under hydrostatic pressure, eigenmodes with fewer circumferential waves and one axial half-wave can be identified as 'most unfavorable' imperfection forms [65]. As shown in Fig. 24, the eigenmodes lead to a much more conservative solution, and thus to less economic designs, than the mean values obtained from the probabilistic modeling approaches. When considering the 99.99 % percentile of the probability distribution, as allowed by EC3, the non-homogeneous approaches also show less conservative results than the homogeneous approach. In addition, the curves of the buckling pressure via the free shell length for the various approaches are depicted in Fig. 25. The curves of the mean buckling pressures from the non-homogeneous approaches (red and blue curve) closely match the measured imperfection (black curve) for all embedment depths. The differences between the two non-homogeneous approaches are very small, which

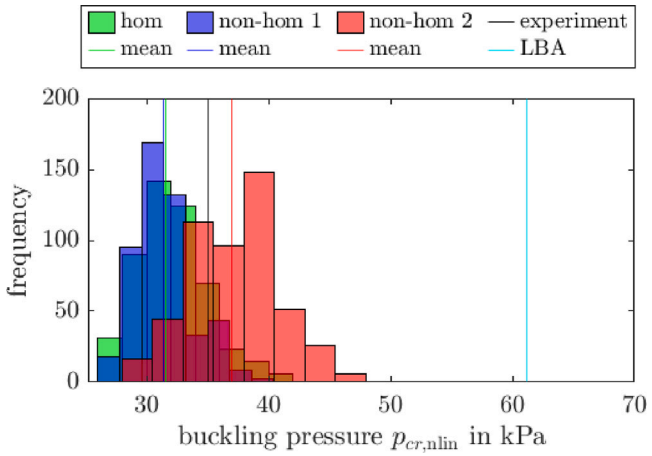

Fig. 21. Histograms (MCS with 500 simulations) of the different imperfection modeling approaches ("hom", "non-hom 1" and "non-hom 2") applied to the lab-scale suction bucket model.

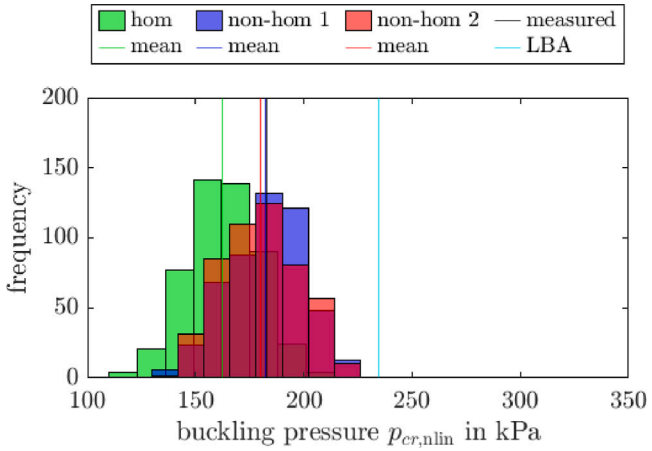

Fig. 22. Histograms (MCS with 500 simulations) of the different random imperfection modeling approaches applied to the full-scale suction bucket model without soil.

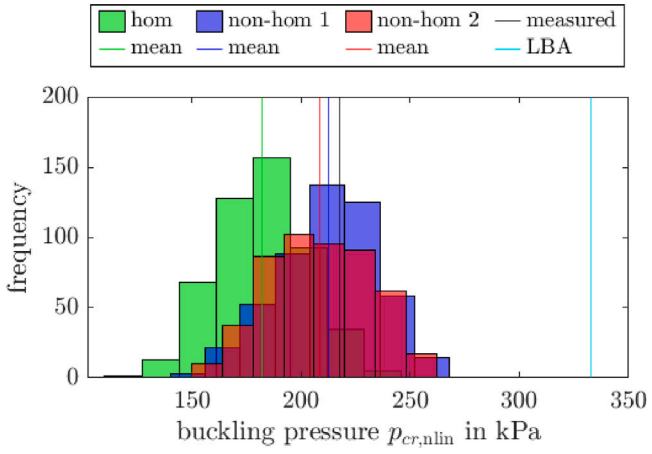

Fig. 23. Histograms (MCS with 500 simulations) of the different imperfection modeling approaches ("hom", "non-hom 1" and "non-hom 2") applied to the full-scale suction bucket model with soil and an embedment depth of 4 m.

confirms that both approaches can accurately capture the obviously non-homogeneous pattern of the full-scale suction bucket as shown in Fig. 19. An interesting observation is that, for larger embedment depths, the homogeneous approach (green curve) approximates the results obtained using the worst eigenmode as the imperfection form (magenta curve) and those obtained using the EC3 reduction factor (orange curve). Furthermore, the differences between the homogeneous approach (green curve) and both non-homogeneous approaches (red and blue curves) increase with increasing embedment depth. This means that modeling random imperfections with a non-homogeneous approach becomes increasingly important when considering the soil.

Finally it should be noted that the definitions regarding the random field properties, such as the Gaussian assumption or the separation of the correlation and variance function into axial and circumferential direction represent significant modeling assumptions. In this context, the manufacturing process of the shells must also be taken into account. The separability of the imperfection field can only be assumed if the field is characterized by a distinct direction, for example due to a rolling direction introduced during fabrication or the presence of weld seams. However, this is not always the case. The Gaussian assumption of the random fields is also a strong modeling choice due to the limited availability of data. This should be further investigated, since a non-Gaussian distributed imperfection field can lead to significantly lower buckling load factors as shown in previous studies for axially compressed shells, see [38,39].

6. Conclusions

This study introduces non-homogeneous random field approaches for more realistic imperfection modeling of suction buckets. Different non-homogeneous variance approaches are proposed based on imperfection measurements of lab- and full-scale suction buckets. Thus, non-homogeneous random imperfections are generated using the Karhunen–Loève expansion for comprehensive probabilistic buckling analyses. The approaches allow to account for imperfections resulting from manufacturing processes, such as welded seams along the skirt of the suction bucket or the variation of imperfection amplitude along the axial direction of the bucket. The novel approaches are compared with a homogeneous random field approach. Buckling responses of the FE models, FEAP and ABAQUS, are compared, validated by experimental tests and verified with an analytical solution.

In summary, the results of the deterministic buckling analysis show that buckling resistance is highly sensitive to different modeling approaches, such as boundary conditions and lid modeling, as demonstrated by the FEAP and ABAQUS models. However, the main finding is that non-homogeneous imperfection modeling can achieve closer agreement with experimental buckling pressures and potentially avoid the large knockdown factors associated with worst-case imperfection design approaches. A homogeneous approach cannot accurately represent all forms of measured imperfection patterns, which show larger deviations at the bottom and, due to the welding of the lid, smaller geometric imperfections at the top for full-scale suction buckets. Furthermore, using a soil model, a study is conducted to analyze the influence of the embedment depth of the suction bucket. Again, the mean buckling pressures from the non-homogeneous approaches closely match the measured imperfections for all embedment depths. The more a suction bucket is embedded, the larger is the difference between the results of homogeneous and non-homogeneous modeling approaches. The embedment depth relevant for design is approximately in the range of $h = 0.25L–0.4L$, where all probabilistic approaches lead to less conservative results than classical approaches, such as using the worst eigenmode or the EC3 reduction factor. Accordingly, one of the key messages of this paper is the recommendation to employ non-homogeneous random field approaches for probabilistic buckling analyses of full-scale suction buckets. The investigated specimens are not assumed to be representative of all fabrication cases. Rather, the study demonstrates that different fabrication protocols and manufacturing characteristics can require different correlation models, which motivates the development

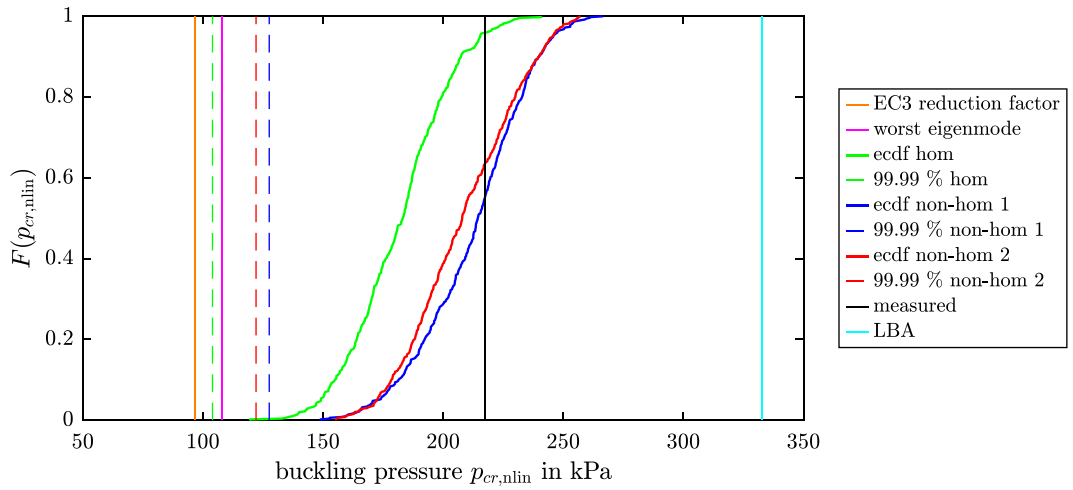

Fig. 24. Comparison of different probabilistic modeling approaches with deterministic design values for the full-scale suction bucket design with an embedment depth of 4 m.

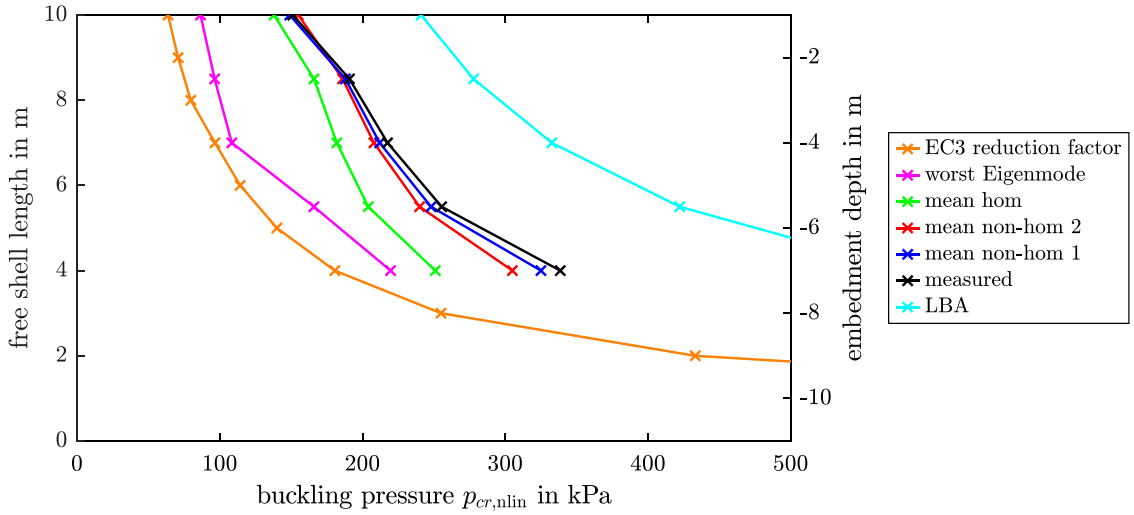

Fig. 25. Buckling pressures via the free shell length of the full-scale bucket for the various modeling approaches.

and application of non-homogeneous approaches. In the case of the lab-scale shell, the second non-homogeneous approach (non-hom 2) can represent the characteristic weld seams, and it avoids non-existent global imperfections, which would lead to overly conservative but unrealistic buckling pressures. However, the mean buckling pressures of the lab-scale suction buckets resulting from this non-homogeneous approach are slightly too high. It should be noted that the sample size of one or two specimens is very small. For a universally applicable approach, the results should be further confirmed using imperfection data from a much larger number of specimens of different types of shells. The proposed methodology can furthermore be scaled to different fabrication quality classes. In practice, the required fabrication quality class is typically defined by the wind farm developer and must subsequently be fulfilled by the fabricator. In the present study, the selected fabrication quality class C serves as an example. For the lab-scale shell, measured imperfection amplitudes are used instead of amplitudes derived from the fabrication quality class to enable direct validation of the simulated buckling pressures against the experimental results.

The study improves stochastic imperfection modeling and proposes a less-conservative, yet experimentally validated, probabilistic design approach. Further research should focus on considering the non-homogeneity of random geometric imperfections in the design optimization of suction buckets. The authors are confident that this can result in substantial material savings, especially since, with the increasing number of planned suction bucket wind farms, the fabrication of suction buckets will move to serial production, and variations within one batch can therefore be represented using the proposed approaches.

Modeling of the imperfections as random fields also allows the consideration of aleatory uncertainties in the optimization process. In this context, uncertainty quantification can be extended through a mixed/hybrid/polymorphic approach to account for epistemic uncertainty (lack of knowledge and imprecision). Furthermore, the introduced non-homogeneous approach can also be further developed. In this study, the non-homogeneity of the variance function is quantified. However, the correlation functions may also depend on the location, and thus can be non-homogeneous. Finally, a design optimization can be performed considering random non-homogeneous imperfections. Thereby, not only geometric parameters such as the thickness, length, or radius of the shell can form the design space, but also stiffeners can be taken into account. Future work should analyze how stiffeners influence the non-homogeneity of random imperfections, which could further optimize suction bucket design.

CRediT authorship contribution statement

M. Fina: Writing – review & editing, Writing – original draft, Visualization, Validation, Software, Resources, Project administration, Methodology, Investigation, Funding acquisition, Formal analysis, Data curation, Conceptualization. **M. Böhm:** Writing – review & editing, Writing – original draft, Visualization, Validation, Software, Methodology, Investigation, Formal analysis, Data curation, Conceptualization. **S. Freitag:** Writing – review & editing, Resources. **P. Schaumann:** Writing – review & editing, Supervision, Resources, Project administration, Funding acquisition. **E. Ghafoori:** Writing – review & editing, Supervision, Resources, Project administration, Funding acquisition.

Declaration of competing interest

The authors declare that they have no known competing financial interests or personal relationships that could have appeared to influence the work reported in this paper.

Acknowledgments

The first author gratefully acknowledges the financial support provided by the Deutsche Forschungsgemeinschaft (DFG, German Research Foundation) under project number 511267658. Furthermore, the authors would like to thank Fraunhofer IWES for conducting the tests on the lab-scale shells within the framework of the ProBucket project, which received financial support by the German Federal Ministry of Economic Affairs and Climate Action (FKZ 03EE3033B).

Data availability

The Fourier coefficients of the geometric imperfections of the full-scale suction bucket and the two lab-scale suction buckets are available open access in the repository of the LUH at https://doi.org/10.25835/jn1a6pxa.

References

[1] G. Costanzo, G. Brindley, P. Tardieu, Wind energy in Europe 2024 Statistics and the outlook for 2025–2030, Tech. rep., windeurope, 2025.

[2] British Standards Institution (BSI), EN 1993-1-6-Eurocode 3: Design of steel structures - Part 1-6: Strength and stability of shell structures, London, 2010.

[3] DNV-RP-C202, Recommended Practice: Buckling Strength of Shells, DNV, Høvik, Norway, 2019.

[4] M. Hilburger, Developing the next generation shell buckling design factors and technologies, in: 53rd AIAA/ASME/ASCE/AHS/ASC Structures, Structural Dynamics and Materials Conference, Honolulu, Hawaii, 2012.

[5] R. Degenhardt, A. Kling, A. Bethge, J. Orf, L. Kärger, R. Zimmermann, K. Rohwer, A. Calvi, Investigations on imperfection sensitivity and deduction of improved knock-down factors for unstiffened CFRP cylindrical shells, Compos. Struct. 92 (8) (2010) 1939–1946, http://dx.doi.org/10.1016/j.compstruct.2009.12.014.

[6] B. Kriegesmann, R. Rolfes, C. Hühne, A. Kling, Fast probabilistic design procedure for axially compressed composite cylinders, Compos. Struct. 93 (12) (2011) 3140–3149, http://dx.doi.org/10.1016/j.compstruct.2011.06.017.

[7] C. Schillo, B. Kriegesmann, D. Krause, Reliability based calibration of safety factors for unstiffened cylindrical composite shells, Compos. Struct. 168 (2017) 798–812, http://dx.doi.org/10.1016/j.compstruct.2017.02.082.

[8] M. Alfano, C. Bisagni, Probability-based methodology for buckling investigation of sandwich composite shells with and without cut-outs, Int. J. Comput. Methods Eng. Sci. Mech. 18 (1) (2017) 77–90, http://dx.doi.org/10.1080/15502287.2016.1276353.

[9] B. Wang, X. Ma, P. Hao, Y. Sun, K. Tian, G. Li, K. Zhang, L. Jiang, J. Guo, Improved knockdown factors for composite cylindrical shells with delamination and geometric imperfections, Compos. Part B: Eng. 163 (2019) 314–323, http://dx.doi.org/10.1016/j.compositesb.2018.11.049.

[10] H.N.R. Wagner, C. Hühne, M. Janssen, Buckling of cylindrical shells under axial compression with loading imperfections: An experimental and numerical campaign on low knockdown factors, Thin-Walled Struct. 151 (2020) 106764, http://dx.doi.org/10.1016/j.tws.2020.106764.

[11] A.J. Sadowski, M.T. Morata, L. Kathirkamanathan, M. Seidel, J.M. Rotter, On the existing test dataset of isotropic cylindrical metal shells under axial compression and the design of modern metal civil engineering shells, Struct. Saf. 102 (2023) 102285, http://dx.doi.org/10.1016/j.strusafe.2022.102285.

[12] R.M.J. Groh, A. Pirrera, Probing the stability landscape of cylindrical shells for buckling knockdown factors, Philos. Trans. R. Soc. A: Math. Phys. Eng. Sci. 381 (2244) (2023) 20220032, http://dx.doi.org/10.1098/rsta.2022.0032.

[13] I. Elishakoff, S. van Manen, P. Vermeulen, J. Arbocz, First-order second-moment analysis of the buckling of shells with random imperfections, AIAA J. 25 (8) (1987) 1113–1117, http://dx.doi.org/10.2514/3.9751.

[14] J. Arbocz, J. Starnes Jr., Future directions and challenges in shell stability analysis, Thin-Walled Struct. 40 (9) (2002) 729–754.

[15] M. Böhm, P. Schaumann, Stochastic modeling of geometric imperfections for buckling analysis of suction buckets, J. Phys.: Conf. Ser. 2362 (1) (2022) 012007, http://dx.doi.org/10.1088/1742-6596/2362/1/012007.

[16] G. Stefanou, Response variability of cylindrical shells with stochastic non-Gaussian material and geometric properties, Eng. Struct. 33 (9) (2011) 2621–2627, http://dx.doi.org/10.1016/j.engstruct.2011.05.009.

[17] M. Broggi, G. Schuëller, Efficient modeling of imperfections for buckling analysis of composite cylindrical shells, Eng. Struct. 33 (5) (2011) 1796–1806, http://dx.doi.org/10.1016/j.engstruct.2011.02.019.

[18] J. Kepple, M. Herath, G. Pearce, G. Prusty, R. Thomson, R. Degenhardt, Improved stochastic methods for modelling imperfections for buckling analysis of composite cylindrical shells, Eng. Struct. 100 (2015) 385–398, http://dx.doi.org/10.1016/j.engstruct.2015.06.013.

[19] K.J. Craig, W.J. Roux, On the investigation of shell buckling due to random geometrical imperfections implemented using karhunen–loève expansions, Internat. J. Numer. Methods Engrg. 73 (12) (2008) 1715–1726, http://dx.doi.org/10.1002/nme.2141.

[20] C. Schenk, G. Schuëller, Buckling analysis of cylindrical shells with random geometric imperfections, Int. J. Non-Linear Mech. 38 (7) (2003) 1119–1132, http://dx.doi.org/10.1016/S0020-7462(02)00057-4.

[21] S. van den Broek, E. Jansen, R. Rolfes, Efficient generation of geodesic random fields in finite elements with application to shell buckling, Thin-Walled Struct. 179 (2022) 109646, http://dx.doi.org/10.1016/j.tws.2022.109646.

[22] M. Böhm, Buckling analysis of suction buckets: Influence of uncertainty in imperfections and soil parameters (Ph.D. thesis), Leibniz University Hannover, 2024, http://dx.doi.org/10.15488/17658.

[23] S. Lauterbach, M. Fina, W. Wagner, Influence of stochastic geometric imperfections on the load-carrying behaviour of thin-walled structures using constrained random fields, Comput. Mech. 62 (5) (2018) 1107–1125, http://dx.doi.org/10.1007/s00466-018-1554-0.

[24] W. Graf, M. Götz, M. Kaliske, Analysis of dynamical processes under consideration of polymorphic uncertainty, Struct. Saf. 52 (2015) 194–201, http://dx.doi.org/10.1016/j.strusafe.2014.09.003.

[25] M. Fina, P. Weber, W. Wagner, A fuzzy stochastic correlation model for geometric imperfections of cylindrical shells, in: 13th International Conference on Applications of Statistics and Probability in Civil Engineering (ICASP13), May 26-30, 2019, Seoul, South Korea, 2019, http://dx.doi.org/10.22725/ICASP13.479.

[26] M. Fina, P. Weber, W. Wagner, Modeling of aleatory and epistemic uncertainties in probabilistic design of cylindrical shells, in: M. Beer, E. Zio (Eds.), Proceedings of the 29th European Safety and Reliability Conference (ESREL), September 22-26, Hannover, Germany, 2019, http://dx.doi.org/10.3850/978-981-11-2724-3_0143-cd.

[27] M. Fina, P. Weber, W. Wagner, Polymorphic uncertainty modeling for the simulation of geometric imperfections in probabilistic design of cylindrical shells, Struct. Saf. 82 (2020) http://dx.doi.org/10.1016/j.strusafe.2019.101894, 101894.

[28] M. Fina, Polymorphe Unschärfemodellierung in der nichtlinearen Strukturmechanik – Stabilität von Schalentragwerken, räumliche Variabilität und Metamodellierung (Ph.D. thesis), Institut für Baustatik, Karlsruher Institut für Technologie, 2020, http://dx.doi.org/10.5445/IR/1000129960.

[29] M. Fina, L. Panther, P. Weber, W. Wagner, Shell buckling with polymorphic uncertain surface imperfections and sensitivity analysis, ASCE-ASME J. Risk Uncertain. Eng. Syst. Part B: Mech. Eng. 7 (2) (2021) http://dx.doi.org/10.1115/1.4050165.

[30] M. Fina, W. Wagner, W. Graf, On polymorphic uncertainty modeling in shell buckling, Computer-Aided Civ. Infrastruct. Eng. 38 (18) (2023) 2632–2647, http://dx.doi.org/10.1111/mice.13054.

[31] M. Schweizer, M. Fina, W. Wagner, S. Freitag, Artificial neural networks for random fields to predict the buckling load of geometrically imperfect structures, Comput. Mech. 76 (2025) 181–204, http://dx.doi.org/10.1007/s00466-024-02595-w.

[32] M. Fina, M.A. Valdebenito, W. Wagner, M. Broggi, S. Freitag, M.G.R. Faes, M. Beer, Control variates method to estimate stochastic buckling loads, Internat. J. Numer. Methods Engrg. 126 (13) (2025) e70070, http://dx.doi.org/10.1002/nme.70070.

[33] M. Fina, C. Lauff, W. Wagner, Optimal shell design with polymorphic uncertain parameters, in: M. Beer, E. Zio, K.-K. Phoon, B. Ayyub (Eds.), Proceedings of the 8th International Symposium on Reliability Engineering and Risk Management, ISRERM, September 4-7, 2022, Hannover, Germany, 2022, http://dx.doi.org/10.3850/978-981-18-5184-1_MS-12-019-cd, Research Publishing.
[34] M. Fina, C. Bisagni, Buckling design optimization of tow-steered composite panels and cylindrical shells considering aleatory and epistemic uncertainties, Comput. Mech. 76 (2025) 59–92, http://dx.doi.org/10.1007/s00466-024-02589-8.
[35] M. Schweizer, M. Fina, W. Wagner, S. Freitag, Optimization of shell structures with fuzzy probability-based random fields using artificial neural networks, in: PAMM, Proc. Applied Mathematics Mech. (PAMM) 25 (4) (2025) e70038, http://dx.doi.org/10.1002/pamm.70038.
[36] M. Fina, C. Bisagni, Neural network-based structural optimization of tow-steered composite panels accounting for polymorphic uncertainty, Compos. Struct. 387 (2026) 120323, http://dx.doi.org/10.1016/j.compstruct.2026.120323.
[37] V. Papadopoulos, G. Stefanou, M. Papadrakakis, Buckling analysis of imperfect shells with stochastic non-Gaussian material and thickness properties, Int. J. Solids Struct. 46 (14) (2009) 2800–2808, http://dx.doi.org/10.1016/j.ijsolstr.2009.03.006.
[38] M. Fina, F. Schietzold, S. Heinzig, S. Freitag, W. Graf, M. Kaliske, Incorporation of non-Gaussian shell imperfections by nataf transformation in efficient random field simulation, in: ESREL 2024 Collection of Extended Abstracts, June 23-27, Cracow, Poland, Polish Safety and Reliability Association, 2024.
[39] F.N. Schietzold, S. Heinzig, M. Fina, W. Graf, S. Freitag, M. Kaliske, Simulation of fuzzy probability based random fields with non-Gaussian marginal distributions by efficient nataf transformation method, in: ESREL 2024 Collection of Extended Abstracts, June 23-27, Cracow, Poland, Polish Safety and Reliability Association, 2024.
[40] S. Geyer, I. Papaioannou, L. Graham-Brady, D. Straub, The spatial averaging method for non-homogeneous random fields with application to reliability analysis, Eng. Struct. 253 (2022) 113761, http://dx.doi.org/10.1016/j.engstruct.2021.113761.
[41] G.A. Fenton, Random field modeling of CPT data, J. Geotech. Geoenvironmental Eng. 125 (6) (1999) 486–498, http://dx.doi.org/10.1061/(ASCE)1090-0241(1999)125:6(486), Cited by: 207.
[42] D.V. Griffiths, J. Huang, G.A. Fenton, Probabilistic slope stability analysis using RFEM with non-stationary random fields, in: Geotechnical Safety and Risk V, IOS Press, 2015, http://dx.doi.org/10.3233/978-1-61499-580-7-704.
[43] S.-H. Jiang, J. Huang, Modeling of non-stationary random field of undrained shear strength of soil for slope reliability analysis, Soils Found. 58 (1) (2018) 185–198, http://dx.doi.org/10.1016/j.sandf.2017.11.006.
[44] V. Papadopoulos, M. Papadrakakis, The effect of material and thickness variability on the buckling load of shells with random initial imperfections, Comput. Methods Appl. Mech. Engrg. 194 (12) (2005) 1405–1426, http://dx.doi.org/10.1016/j.cma.2004.01.043, Special Issue on Computational Methods in Stochastic Mechanics and Reliability Analysis.
[45] C. LeBlanc Bakmar, Design of Offshore Wind Turbine Support Structures: Selected topics in the field of geotechnical engineering (Ph.D. thesis), (18) Department of Civil Engineering, Aalborg University, Denmark, 2009.
[46] A.J. Sadowski, M. Seidel, H. Al-Lawati, E. Azizi, H. Balscheit, M. Böhm, L. Chen, I. van Dijk, C. Doerich-Stavridis, O.K. Fajuyitan, A. Filippidis, A.W. Fischer, C. Fischer, S. Gerasimidis, H. Karampour, L. Kathirkamanathan, F. Marten, Y. Mihara, S. Mishra, V. Sakharov, A. Shahini, S. Subramanian, C. Topkaya, H.N.R. Wagner, J. Wang, J. Wang, K.K. Yadav, X. Yun, P. Zhang, 8-MW wind turbine tower computational shell buckling benchmark. Part 1: An international 'round-robin' exercise, Eng. Fail. Anal. 148 (2023) 107124, http://dx.doi.org/10.1016/j.engfailanal.2023.107124.
[47] A. Foglia, T. Quiroz, V. Widerspan, D. Heinrich, G. Binsker, A. Schenk, I. Sanders, M. Achmus, M. Collmann, M. Böhm, P. Schaumann, W. Elsesser, B. Schädlich, F. Kirsch, T. Richter, M. Gose, P. Pehl, P. Kleineidam, J. Maas, S. Ibis, K. Oltmann, Aktuelle untersuchungen an suction buckets für offshore-windenergieanlagen – das ProBucket-projekt, Bautechnik 99 (9) (2022) 669–678, http://dx.doi.org/10.1002/bate.202200065.
[48] J. Arbocz, H. Abramovich, The initial imperfection data bank at the delft university of technology: Part i, 1979.
[49] J. Arbocz, J.G. Williams, Imperfection surveys on a 10-ft-diameter shell structure, AIAA J. 15 (7) (1977) 949–956, http://dx.doi.org/10.2514/3.7389.
[50] B. Sudret, A.D. Kiureghian, Stochastic finite element methods and reliability – a state-of-the-art report, 2000.
[51] E. Vanmarcke, Random Fields: Analysis and Synthesis, World Scientific, Singapore, 2010.
[52] F. Schietzold, A. Schmidt, M. Dannert, A. Fau, R.M.N. Fleury, W. Graf, M. Kaliske, C. Könke, T. Lahmer, U. Nackenhorst, Development of fuzzy probability based random fields for the numerical structural design, GAMM-Mitt. 42 (1) (2019) e201900004, http://dx.doi.org/10.1002/gamm.201900004.
[53] M. Baitsch, Optimierung druckbeanspruchter Stabtragwerke unter Berücksichtigung geometrischer Imperfektionen (Ph.D. thesis), Lehrstuhl für Ingenieurinformatik im Bauwesen, Ruhr-Universität Bochum, 2003.
[54] M.L. Stein, Interpolation of Spatial Data – Some Theory for Kriging, Springer-Verlag New York, 1999.
[55] C. Rasmussen, C. Williams, Gaussian Processes for Machine Learning, The MIT Press, 2005, http://dx.doi.org/10.7551/mitpress/3206.001.0001.
[56] P. Hansen, V. Pereyra, G. Scherer, Least Squares Data Fitting with Applications, Johns Hopkins University Press, 2013.
[57] W. Wagner, P. Wriggers, A simple method for the calculation of postcritical branches, Eng. Comput. 5 (2) (1988) 103–109.
[58] W. Wagner, A note on FEM buckling analysis, Commun. Numer. Methods Eng. 11 (2) (1995) 149–158, http://dx.doi.org/10.1002/cnm.1640110208.
[59] Dassault Systemes, AbaqUS, 2019, http://www.3ds.com.
[60] R.L. Taylor, Finite element analysis program (FEAP), 2025, http://www.ce.berkeley.edu/projects/feap/.
[61] W. Wagner, F. Gruttmann, A robust non-linear mixed hybrid quadrilateral shell element, Internat. J. Numer. Methods Engrg. 64 (5) (2005) 635–666, http://dx.doi.org/10.1002/nme.1387.
[62] S. Klinkel, F. Gruttmann, W. Wagner, A mixed shell formulation accounting for thickness strains and finite strain 3d material models, Internat. J. Numer. Methods Engrg. 74 (6) (2008) 945–970, http://dx.doi.org/10.1002/nme.2199.
[63] F. Gruttmann, W. Wagner, An advanced shell model for the analysis of geometrical and material nonlinear shells, Comput. Mech. 66 (2020) 1353–1376, http://dx.doi.org/10.1007/s00466-020-01905-2.
[64] Offshore Wind Farm Construction Method Statement, Tech. Rep. LF000009-CST-OF-MST-0001, Seagreen Wind Energy Ltd, 2023.
[65] M. Böhm, P. Schaumann, E. Ghafoori, Shell buckling of suction buckets for offshore wind turbines considering imperfection and soil parameter sensitivity, Eng. Struct. 302 (2024) 117310, http://dx.doi.org/10.1016/j.engstruct.2023.117310.
[66] A. Wolmir, Biegsame Platten und Schalen, VEB Verlag für Bauwesen, Berlin, 1962.
[67] X. Yun, L. Gardner, Stress-strain curves for hot-rolled steels, J. Constr. Steel Res. 133 (2017) 36–46, http://dx.doi.org/10.1016/j.jcsr.2017.01.024.
[68] Deutsches Institut für Normung e.V. (DIN), DIN EN 1993-1-5-Eurocode 3: Design of steel structures–Part 1-5: Plated structural elements, Berlin, 2019.
[69] British Standards Institution (BSI), EN 1990 Eurocode 0: Basis of structural design, London, 2010.